

**Metamorphic evolution and Zircon ages of pelitic granulites
in eastern Hebei, North China Craton: Insights into the
regional Archean P-T-t history**

Zhanzhan Duan ^a, Chunjing Wei ^{a,*}, Hafiz Ur Rehman ^b

^a*MOE Key Laboratory of Orogenic Belts and Crustal Evolution, School of Earth and Space*

Sciences, Peking University, Beijing, 100871, China;

^b*Graduate School of Science and Engineering, Kagoshima University, Korimoto 1-21-35,*

Kagoshima 890-0065, Japan;

* Corresponding author: Chunjing Wei

Tel: +86 13651355549

E-mail address: cjwei@pku.edu.cn

ABSTRACT

Archean supracrustal granulites occur as localized slivers or rafts in granitoids, and this particular occurrence of supracrustal granulites has not been much concerned from the perspective of metamorphic evolution. The pelitic granulites in eastern Hebei occur as slivers in TTG gneisses and charnockite. Three pelitic granulite samples

involving orthopyroxene–garnet gneiss (JD1334), biotite–garnet gneiss (JD1453) and sillimanite–garnet gneiss (JD15126) were collected from Taipingzhai and Laolijia areas. Based on textural observations and mineral compositions, four generations of assemblages involving final, peak, inclusion and overprinting stages are identified. The observed final assemblage yield P–T conditions of 8.0–9.5 kbar/870–890 °C. The observed peak assemblage characteristic of the absence of the matrix biotite record condition of $T > 950$ °C with fixed $P = 9$ kbar. An isobaric cooling path from peak to final assemblage is constrained by mineral isopleths. The inclusion assemblages characterized by plagioclase inclusions with high X_{An} contents are predicted to be stable at low pressure and/or high temperature field. They form an anticlockwise P–T path. The overprinting assemblage characteristic of coronary garnet (g_2) coexisting with fine-grained mineral aggregates defines P–T condition of 10–12 kbar/830–880 °C. The deposition age of the sedimentary protolith of pelitic granulites was ~2.5 Ga, coeval with the crystallization age of TTG gneisses. Both of them were later subjected to granulite facies metamorphism at ~2.48 Ga. The Archean anticlockwise P–T paths suggest a tectonic scenario to explain the particular occurrence of the Archean supracrustal granulites. Firstly, supracrustal sediments experienced thermal event under low pressures attributed to the intrusion of high-temperature TTGs, resulting in dehydrations of hydrous phases. Then, the dried metasediments interlayered with iron-bearing formations potentially denser than the surrounding lithologies tend to drop into the TTG magma ocean, causing the pressure-increase in the metasediments. Thirdly, the dropped metasediments

experienced cooling process under lower crust in coupled with the crystallization of the surrounding TTG magma to form the observed final assemblages. Finally, they uplifted as a consequence of the doming processes in Archean terranes.

Keywords: pelitic granulite; zircon dating; metamorphic P–T path; eastern Hebei; North China Craton

1. Introduction

The Archean terranes are dominantly composed of granitoids of tonalite–trondhjemite–granodiorite (TTG) compositions and supracrustal rocks, and are divided into low- and high-grade domains according to metamorphic grades (Condie, 1981). The low-grade or granitoid-greenstone terrains are prevailed with the large-scale development of “dome-and-keel” structures where the greenstone belts occur as synclinal keels among granitoid domes (e.g. Kröner, 1984; Campbell and Hill, 1988; Collins et al., 1998; Bleeker, 2002; Lin and Beakhouse, 2013). The metamorphic grade of Archean greenstone rocks ranges from greenschist- to amphibolite-facies, and higher grades typically occur around the margins of greenstone belts, probably caused by intrusion of plutons (Boniface and Mruma, 2012). In contrast, the high-grade terrains are characteristic of the development of granulites. Brown (2007) summarized the peak P–T conditions of granulites from twenty Archean terranes, where nine of them fall into ultrahigh-temperature (UHT) type with P–T conditions of 9–14 kbar/950–1100 °C, eight of them into normal

granulite type with P–T conditions of 6.5–9.9 kbar/880–950 °C and three of them into medium-temperature eclogite–high-pressure granulite type with P–T conditions of 11–17.5 kbar/700–880 °C. It seems that the Archean granulites are dominated by UHT type. In some Archean high-grade terrains, supracrustal granulites occur as slivers or rafts of tens to thousands square meters in granitoids, for instance, the supracrustal rocks from the Akia and the Tasiusarsuaq terranes in southern West Greenland (Riciputi et al., 1990), the Vedlozero–Segozero high-grade greenstone belts in Karelian Province (e.g. Käyhö et al., 2007), the Sargur Group in Western Dharwar Craton (e.g. Peucat et al., 1993; Ghosh et al., 2004) and the supracrustal granulites of North China Craton (NCC) exposed in eastern Hebei (Wu et al., 1998). This particular occurrence of the Archean supracrustal granulites has not been too much concerned especially from a point of view of metamorphic evolution.

The temperature conditions of granulites are commonly underestimated using conventional Fe–Mg exchange thermometers due to the fast cation diffusion during cooling (Frost and Chacko, 1989; Harley, 1989; Powell and Holland, 2008). An alternative approach using the Al-solubility in orthopyroxene in equilibrium with garnet proposed by Pattison et al. (2003) can correct the effect of late Fe–Mg exchange to some extent. However, it cannot be widely applied to rocks without the specific mineral assemblages. Recently, pseudosection thermobarometry is increasingly used to determine the P–T conditions of granulites, which typically yields higher peak temperature estimates because it uses the assemblage as the basis for estimating P–T conditions and the assemblage is less prone to post-peak

modification than mineral compositions (e.g. White et al., 2002; Kelsey et al., 2003; Korhonen et al., 2013). However, as granulite metamorphism is commonly concomitant with melt, the post-peak metamorphic (or retrograde) reactions with melt may modify the mineral modes and compositions and even cause the scenario that the preserved 'peak' assemblages in granulites commonly represent the retrograde solidus conditions, rather than the real peak conditions that the rock has reached (White and Powell, 2002; Korhonen et al., 2013; Li and Wei, 2016). The assemblages on the retrograde fluid-absent solidus in granulites are nominated as final assemblages, which can be differentiated from the peak assemblages through detailed petrographic observations (Korhonen et al., 2013). Generally, some components, such as, anorthite of plagioclase, grossular of garnet and Ti in biotite, that are less affected by diffusion are significant for constraining the peak P–T conditions of granulites (Li and Wei, 2016).

The Eastern Hebei terrane is located at the northwestern part of the NCC Eastern Block and comprises predominantly Neoproterozoic metamorphic basement, which are overlain at their periphery by Mesoproterozoic to Mesozoic cover sequences, and are intruded by several Mesozoic granitic plutons (e.g. Yang et al., 2008; Li et al., 2010; Nutman et al., 2011; Zhao and Zhai, 2013). The Neoproterozoic basement is composed of TTG gneisses, granitoid plutons and supracrustal rocks (Fig. 1a), and the intrusive rocks of 2.6–2.5 Ga cover 80–70% of the surface (e.g. Geng et al., 2006, 2012; Yang et al., 2008; Li et al., 2010; Nutman et al., 2011; Zhao and Zhai, 2013; Bai et al., 2014, 2015). In Taipingzhai region, the TTG gneisses and supracrustal rocks were

considered to have been subjected to granulite-facies metamorphism in Neoproterozoic time with an anticlockwise cooling P–T path (Zhao et al., 1998). Using conventional thermobarometers, the peak P–T conditions for mafic granulites in the supracrustal sequences were estimated to be 9–11 kbar/810–940 °C (He and Ye, 1992), 9.5 kbar/780–816 °C (Chen and Li, 1996) and 8–8.5 kbar/850–900 °C (Zhao et al., 1998). Recently, the mafic granulites and charnockite at Taipingzhai were estimated using pseudosection modelling with THERMOCALC, giving 9.6–10.3 kbar/860–900 °C (Kwan et al., 2016) and 7–14 kbar/800–920 °C (Yang et al., 2015) for the peak conditions, similar to the results from the conventional thermometers. However, there have been no data available for pelitic granulites in eastern Hebei.

In this paper, we present systematic data of petrography, major element compositions, LA-ICP-MS zircon U–Pb ages and phase modelling results for pelitic granulites from eastern Hebei to elucidate their metamorphic evolution and geological significance.

2. Geological setting

The North China Craton is one of the oldest cratonic blocks on Earth, containing crustal rocks up to ~3.85 Ga (Liu et al., 1992; Song et al., 1996; Liu et al., 2007, 2008). The Precambrian basement of the NCC can be divided into high-grade gneiss complexes and low- to medium-grade granite-greenstone belts that are widespread over the whole NCC (Zhao and Zhai, 2013). For the past decade, it has been widely accepted that the NCC is subdivided into Western Block and Eastern Block that are

welded along the Trans-North China Orogen (TNCO), although the timing and tectonic processes involved in the amalgamation of the two blocks remains controversial (e.g. Zhao et al., 1998, 2001, 2005, 2012; Zhao and Zhai, 2013; Santosh et al., 2012; Liu et al., 2012; Wilde et al., 2002, 2005; Wei et al., 2014).

The early Precambrian Eastern Hebei terrane can be divided into five litho-tectonic units after Wu et al. (1998): (I) the Zunhua high-grade meta-greenstone belt, (II) Taipingzhai granulite facies unit, (III) Qian'an gneiss dome region, (IV) Luanxian amphibolite-facies and (V) Qinglong amphibolite/greenschist-facies metamorphic belts (Fig. 1b). The Zunhua high-grade meta-greenstone belt is composed mainly of supracrustal rocks and orthogneiss (Wu et al., 1998; Geng, 1998; Geng et al., 2006; Zhai and Liu, 2001; Nuttman et al., 2011, 2014; Guo et al., 2013, 2015; Liu et al., 2014; Bai et al., 2015). These supracrustal rocks were metamorphosed under granulite-facies conditions and comprised metasedimentary rocks, Banded Iron Formations (BIF) and metavolcanic rocks that were dated at 2.61–2.52 Ga (Guo et al., 2013). Wall rocks from the Shirengou BIF deposit, comprising hornblende plagioclase gneisses and plagioclase amphibolites, have magmatic crystallization ages of 2.55–2.54 Ga (Zhang et al., 2012). Recent investigations based on progressive zircon U–Pb dating methods reveal that most of these orthogneisses series have Neoproterozoic magmatic precursors that were dated at 2.55–2.50 Ga (e.g. Geng et al., 2006; Nuttman et al., 2011; Guo et al., 2013; Bai et al., 2014, 2015). The Taipingzhai granulite-facies unit consists of TTG gneisses, charnockite and supracrustal rocks (Wu et al., 1998). The magmatic precursors of the TTG gneisses and charnockite were emplaced

between 2.53–2.49 Ga and 2.55–2.52 Ga, respectively, which were followed by regional granulite-facies metamorphism at 2.45–2.42 Ga (Geng et al., 2006; Bai et al., 2015). The supracrustal rocks including mafic, pelitic granulites and magnetite quartzites occur as slivers of hundreds to thousands of meters in the extensive TTG gneisses (Figs. 2 and 3a). The Qian'an gneiss dome, which is surrounded by supracrustal residues of Paleo-Mesoarchean in its southwest border, is composed mainly of tonalitic-granodioritic gneisses of amphibole to granulite facies metamorphism. Detrital zircon grains obtained from fuchsite-bearing quartzite in these supracrustal residues show ages > 3.85 Ga (Liu et al., 1992; Wilde et al., 2008; Nuttman et al., 2011, 2014). Most orthogneisses that were metamorphosed in amphibole/granulite-facies were dated 2.55–2.51 Ga, but a few emplaced at 3.28–2.94 Ga (Nuttman et al., 2011, 2014). The Luanxian amphibolite-facies belt is composed of a volcano-sedimentary series that was grouped as the Luanxian Group (Qian et al., 1985), and a number of tonalitic-granodioritic gneisses that were dated with an emplacement age of 2.55–2.53 Ga (Geng et al., 2006). The Qinglong amphibolite/greenschist-facies belt consists of turbiditic sediments interlayered with basic and acidic volcanics grouped as the Shuangshanzi Group (amphibolite-facies) and Zhuzhangzi Group (greenschist-facies). Some researchers interpreted the Shuangshanzi and Zhuzhangzi Groups as Paleoproterozoic products in the previous studies (e.g. Sun, 1984; Qian et al., 1985). In addition, Liu et al. (2014) reported that the sedimentation of the Shuangshanzi Group began at ~ 2.35 Ga which were evidenced by the crystallization age of 2352 ± 4 Ma of a meta-porphyritic dacite and

the youngest detrital zircon age peaks of 2337–2329 Ma from the Shuangshanzi Group, and the youngest age peaks of 2331–2329 Ma have also been identified from the overlying Zhuzhangzi Group. Alternatively, both Shuangshanzi and Zhuzhangzi Groups were proven to be actually deposited at the end of the Neoproterozoic, based on zircon ages of 2.56–2.50 Ga from the low-grade metasedimentary rocks (Sun et al., 2010; Lü et al., 2012; Guo et al., 2015), and represent sedimentary covers in an intra-continental rift basin after the ~2.5 Ga cratonization (e.g. Zhai, 2011; Lü et al., 2012). A few mafic dykes were described cross-cutting the Archean TTG gneisses and supracrustal rocks in the Zunhua meta-greenstone belt and the Taipingzhai complex (Chen, 1990; Song, 1990), which were determined to have experienced high pressure granulite-facies metamorphism in ~1.82 Ga (Duan et al., 2015).

The studied pelitic granulites from the Taipingzhai granulite-facies unit are interlayered with magnetite quartzite and two-pyroxene granulites (Fig. 3a). They are intensively partial melted with leucosomes of several millimeters wide (Fig. 3b).

3. Petrological analyses

3.1 Analysis method

The bulk-rock compositions of the pelitic granulites were determined by ICP-OES analysis at China University of Geoscience (Beijing). Microprobe analyses of minerals were performed using a JXA-8100 microprobe at the Laboratory of Orogenic Belt and Crustal Evolution of Peking University. The analyses were conducted under conditions of 15 kV accelerating voltage, a 10-nA current with a

beam diameter of 2 μm . Natural and synthetic minerals of SPI Company were used for standardization. Compositional X-ray maps of garnet were obtained with an energy dispersive X-ray spectrometry of Oxford INCA X-MAX50 250 +, installed on a scanning electron microscope (SEM) of FEI Quanta 650 FEG. The running condition was set to a 20 kV acceleration voltage and spot 5 beams current.

3.2 Bulk-rock compositions

Three samples (JD1334, JD1453 and JD15126) were selected from the Taipingzhai and Louzishan areas (Fig. 2). Their locations, main mineral components and modal proportions are listed in Table 1, and bulk-rock compositions are presented in Table 2. They show $\text{SiO}_2 = 58.32\text{--}62.74$ (wt.%), $\text{Al}_2\text{O}_3 = 16.60\text{--}17.41$, $\text{CaO} = 2.20\text{--}3.46$, $\text{Na}_2\text{O} = 2.23\text{--}3.68$, $\text{K}_2\text{O} = 1.65\text{--}2.19$, $\text{A/CNK} = 1.23\text{--}1.70$, and $\text{Mg}^\# = 30\text{--}52$, indicating CaO-rich and K₂O-poor pelitic compositions.

3.3 Petrography and mineral chemistry

Pelitic granulites are porphyroblastic with garnet or occasionally with plagioclase porphyroblasts in a foliated matrix consisting of plagioclase, K-feldspar, quartz and minor biotite and ilmenite with or without orthopyroxene and sillimanite.

Representative mineral analyses are listed in Tables 3 and 4. Field and micrographs of representative pelitic granulites are shown in Figs. 3–4 and representative mineral chemistry is presented in Fig. 5.

Sample JD1334 is an orthopyroxene-bearing pelitic granulite in which garnet can be divided into two types. Type-1 garnet (g_1) occurs as subhedral to anhedral porphyroblasts of 0.5–2 mm across and contains inclusions of quartz and ilmenite,

whereas type-2 garnet (g_2) occurs as coronae around porphyroblastic garnet (Fig. 3c). Type-1 garnet contains 67–68 mol.% almandine, 25–27 mol.% pyrope, 5–7 mol.% grossular and ~1 mol.% spessartine, and shows weak zoning with core-rim increasing in grossular from 5 to 7 mol.% (Fig. 5a). Type-2 garnet shows higher grossular of 10–13 mol.% than type-1 (Fig. 5a and Table 3). Plagioclase is divided into two types on the basis of grain sizes. The coarse-grained plagioclase is anhedral and 0.2–0.5 mm across in the matrix (Fig. 3d), showing core-rim decreasing in X_{An} [=Ca/(Ca + Na + K)] from 0.31 to 0.26 (Fig. 5f). The fine-grained plagioclase is of 0.02–0.06 mm across with little lower X_{An} of 0.24–0.29, and forms aggregates with quartz, biotite and K-feldspar (Fig. 3e). Biotite occurs as medium-grained flakes of 0.1–0.3 mm long in the matrix with X_{Mg} [=Mg/(Mg + Fe²⁺)] of 0.56–0.59 and Ti = 0.29–0.32 p.f.u. These biotite flakes show irregular shapes formed along grain boundaries, or as pressure shadows of garnet (Fig. 3e), indicating of later generation. Orthopyroxene occurs as anhedral grains of 0.1–0.5 mm across and is fairly homogeneous in chemical composition with X_{Mg} [=Mg/(Mg + Fe²⁺)] of 0.52–0.53. K-feldspar occurs as medium-grained tabular crystals in the matrix, with Ab = 0.09–0.11 and Or = 0.89–0.91. Based on the textural observation and mineral compositions presented above, three generations of assemblages involving final, peak and overprinting of metamorphism can be identified. The final assemblage mainly consists of type-1 garnet, orthopyroxene, K-feldspar, plagioclase (coarse-grained), biotite, quartz and ilmenite, and the peak assemblage is characteristic of the absence of the matrix biotite. The overprinting assemblage consists of type-2 garnet, aggregates of quartz, biotite,

K-feldspar and plagioclase (fine-grained).

Sample JD1453 is a pelitic granulite with higher amounts of plagioclase and biotite than in the other samples. Garnet occurs as porphyroblasts of 1–5 mm across. It contains $X_{alm} = 0.52–0.57$, $X_{py} = 0.37–0.41$, $X_{gr} = 0.04–0.08$ and $X_{sp} = 0.01$. A few large garnet grains of 4–5 mm across contain numerous inclusions of plagioclase and a few grains of quartz (Fig. 4a) and show higher X_{gr} of 0.07–0.08 in the core and mantle than in the rim (Fig. 5b). However, most medium-coarse garnet grains of 1–3 mm across contain a few inclusions of quartz (Fig. 4b) and show lower X_{gr} of 0.04 without any change from core to rim (Fig. 5c). Garnet commonly develops an outer rim that is higher in X_{gr} and lower in X_{py} than in the inner rim (Fig. 5c), similar to the overprinting garnet (g_2) in sample JD1334. Biotite occurs as small flakes of irregular shapes in the matrix, and commonly forms in the pressure shadows of garnet, showing $X_{Mg} = 0.62–0.64$ and $Ti = 0.31–0.33$. A few biotite flakes are formed along the cracks in garnet (Fig. 4b) and shows higher X_{Mg} of 0.73 and lower $Ti = 0.28$ p.f.u. than in the matrix grains, interpreted to be formed under low temperature with fluid infiltration. Plagioclase occurs as anhedral grains of 0.3–3 mm across in the matrix (Fig. 4e) or as rounded inclusions of 0.1–0.4 mm across in garnet (Fig. 4a). Plagioclase in the matrix has X_{An} of 0.29–0.31 without clear zoning (Fig. 5g1), whereas plagioclase inclusions in garnet have higher X_{An} of 0.43–0.45 (Fig. 5g2). K-feldspar occurs as medium-grained anhedral grains in the matrix, with $Ab = 0.05–0.07$ and $Or = 0.93–0.95$. Based on the textural relations and mineral compositions presented above, four generations of assemblages involving final, peak, inclusion and overprinting of

metamorphism can be identified. The peak assemblage is observed to include garnet (g_1), K-feldspar, plagioclase, quartz and ilmenite, the final assemblage is characteristic of the formation of the matrix biotite together with other minerals observed in the peak assemblage. The inclusion and overprinting assemblages are characterized by plagioclase with high X_{An} (0.43–0.45) and garnet with high grossular content (g_2), respectively.

Sample JD15126 is a sillimanite-bearing pelitic granulite with good foliation defined by oriented sillimanite, biotite and plagioclase. Garnet occurs as anhedral or subhedral porphyroblasts of 0.5–2 mm across and contains $X_{alm} = 0.56–0.58$, $X_{py} = 0.37–0.41$, $X_{gr} = 0.03–0.05$ and $X_{sp} = 0.00–0.01$. Garnet has inclusions of plagioclase and shows little higher X_{gr} in the core than garnet without plagioclase inclusions (Figs. 5d, e). Both of them show flat profiles of X_{gr} in the core but decreasing in the narrow rim section (g_1) and are locally surrounded by Ca-rich garnet corona (g_2 , Figs. 4d, 5d, e). Biotite occurs as small fibers of irregular shapes in the matrix, and commonly forms in the pressure shadows of garnet, showing $X_{Mg} = 0.75$ and $Ti = 0.27–0.30$. Plagioclase occurs as anhedral grains of 0.3–0.8 mm across in the matrix (Fig. 4f) or as rounded inclusions of 0.1–0.3 mm across in garnet (Fig. 4d). Most plagioclase grains in the matrix are not significantly zoned relative to X_{An} , and a few grains show core-rim zoning with X_{An} decreasing from 0.34 to 0.30 in the matrix (Fig. 5h1). The plagioclase inclusions in garnet show core-rim zoning with X_{An} decreasing 0.49–0.47 (Fig. 5h2). Sillimanite exhibits oriented columnar and granular crystals in the matrix. K-feldspar occurs as tabular crystals in the matrix, with $Ab = 0.09–0.10$ and $Or =$

0.89–0.91. Based on the textural observation and mineral compositions presented above, the observed peak assemblage contains garnet (g_1), K-feldspar, sillimanite, plagioclase, quartz and rutile, the final assemblage is characteristic of the formation of the matrix biotite together with the other minerals observed in the peak assemblage. The inclusion and overprinting assemblages are characterized by plagioclase with high X_{An} (0.47–0.49) values and Ca-rich garnet (g_2) than inner rim, respectively, same as sample JD1453.

In addition, the overprinting of garnet in some samples presents fantastic coronae around the early-stage garnet porphyroblasts (Fig. 3f).

4. Phase equilibria modelling using pseudosections

Based on the mineral assemblages and compositions for samples JD1334, JD1453 and JD15126 mentioned above, the model system (Mn)NCKFMASHTO ($MnO-Na_2O-CaO-K_2O-FeO-MgO-Al_2O_3-SiO_2-H_2O-TiO_2-Fe_2O_3$) was chosen to calculate P–T and T–M(H_2O) pseudosections. This system provides the most realistic compositional approximation to the studied rocks within which suprasolidus conditions can be calculated (White et al., 2007). Pseudosection calculations were performed using THERMOCALC 3.33, using the October 2009 updated version of the Holland and Powell (1998) dataset (files tcds55.txt). Mineral activity–composition relationships are those defined for silicate melt (White et al., 2007), biotite (White et al., 2007), cordierite (Holland and Powell, 1998), garnet (White et al., 2005, 2007), orthopyroxene (White et al., 2002), plagioclase and K-feldspar (Holland and Powell,

2003) and ilmenite (White et al., 2000). Kyanite/sillimanite, rutile and quartz are pure end-member phases.

The whole-rock chemical compositions obtained by ICP-OES analysis for a piece of rock generally cannot be used to model well the phase equilibria observed in a thin-section because of (1) fractionation consequent to the growth of porphyroblasts, commonly evident as zoned minerals, (2) the heterogeneous accumulation of some minerals (e.g. mica-rich folia), and (3) the effect of retrograde metamorphism. The effective bulk-rock compositions would be better when modelling phase diagrams than the whole-rock chemical compositions. The effective bulk-rock compositions were generated according to mass balance constraints by integrating mineral compositions and modal abundance data for the phases present (Carson et al., 1999). The modal abundance for each mineral was obtained by point-counting. In addition, the H₂O content used in the modelling is adjusted using T–M(H₂O) (referring to the H₂O mol.% in a rock) diagrams so that the final phase assemblage is stable just above the solidus (Korhonen et al., 2013). The effective bulk-rock compositions for the calculated pseudosections are listed in Table 2.

Sample JD1334

A P–T pseudosection is calculated using an effective bulk-rock composition on the basis of the final assemblage for K-feldspar, plagioclase, quartz and ilmenite in excess with the P–T window of 2–13 kbar and 700–1100 °C (Fig. 6). The solidus is predicted at temperatures between 760 and 870 °C. Biotite-out occurs at temperatures

just above the solidus. Cordierite is stable at pressures less than ~5 kbar.

The observed final assemblage $g\text{-bi-opx-ksp-pl-q-ilm(-liq)}$ is quadrivariant in the model system and defines a narrow temperature range of 865–870 °C under a fixed pressure of 9 kbar. The measured $X_{py} = 0.26\text{--}0.27$ in the core and mantle of garnet (g_1) and the $X_{Mg\text{-bi}} = 0.59$ in the matrix biotite are plotted in the stability field for the final assemblage, but the measured X_{py} of 0.25 in the rims of g_1 is plotted in the subsolidus fields. The measured $X_{Mg\text{-opx}} = 0.52\text{--}0.53$ is predicted to mostly reflect cooling conditions as the $X_{Mg\text{-opx}}$ increases with cooling in the subsolidus fields. The observed biotite-absent peak assemblage $g\text{-opx-ksp-pl-q-ilm(-liq)}$ is univariant in the model system and defines a wide P–T range of 5.0–12 kbar and 825–1090 °C. The measured core-rim zoning of increasing X_{gr} (0.05→0.07) and decreasing X_{An} (0.31→0.26) are modelled to be consistent with a cooling path, where the isopleths of the maximum X_{An} and minimum X_{gr} from grains cores define a P–T condition of ~1050 °C and 9.8 kbar. The P–T estimate has uncertainties of ~0.4 kbar and ~24 °C (two-sigma level) calculated with THERMOCALC for the X_{An} and X_{gr} isopleths, respectively. However, such uncertainties should be considered a minimum as they are propagated from the uncertainties on the enthalpy alone and do not include other sources of uncertainty. The predicted Ti content in biotite is only 0.18 p.f.u. at temperatures on the biotite-out, significantly lower than the measured values (Ti = 0.26–0.32 p.f.u.). From the above-mentioned, an isobaric cooling path can be inferred as shown in Fig. 6. On the basis of the changes of phase modes and compositions calculated (Table 5), metamorphic evolution is dominated by melt crystallization via

liq = g + ksp + pl + opx + q + ilm in the P–T field of the peak assemblage, followed by ksp + opx + ilm + liq = g + q + pl + bi in the narrow field of the final assemblage. It is noted that the observed mineral modes are roughly consistent with the predicted values at point B on the solidus. Further cooling under the subsolidus is predicted by exchange reactions causing Mg-rich in biotite and orthopyroxene and Fe-rich in garnet.

For modelling the P–T evolution of the overprinting assemblage, an effective bulk rock composition was generated according to the equilibria in local domains by assuming type-2 garnet (g_2) to be ~10 vol. % and the modal abundance for other minerals to be their original proportions in the final assemblage. Its effective bulk-rock composition is listed in Table 2. A P–T pseudosection is calculated for K-feldspar, plagioclase, quartz and ilmenite in excess (Fig. 7). The observed overprinting assemblage g–bi–ksp–pl–q–ilm(–liq) defines a P–T range of 10–12 kbar and 830–880 °C, consistent with the predictions from the measured $X_{An} = 0.24–0.29$ in the fine-grained plagioclase and the type-2 garnet compositions with higher $X_{py} = 0.22–0.23$ and $X_{gr} = 0.12–0.13$.

Sample JD1453

The P–T pseudosection calculated for sample JD1453 is drawn for plagioclase and quartz in excess with the P–T window of 2–12 kbar and 750–1150 °C (Fig. 8). The fluid-absent solidus occurs at temperatures about 850–870 °C under pressure of 5–10 kbar. The observed final assemblage g–bi–ksp–pl–q–ilm(–liq) is quadrivariant in

the model system and defines a P–T range of 7.0–9.5 kbar and 860–900 °C. The measured $X_{py} = 0.38–0.41$ and $X_{gr} = 0.04–0.08$ in garnet and $X_{An} = 0.29–0.31$ in the matrix plagioclase are predicted to yield P–T conditions roughly consistent with the stability of the final assemblage, but the plagioclase compositions suggest higher temperature in orthopyroxene-stability fields. The measured X_{Mg-bi} of 0.62–0.64 from the matrix biotite could reflect lower pressure and temperature cooling conditions, while the predicted Ti content in biotite is only 0.22 p.f.u. at the biotite-out temperature, significantly lower than the measured $Ti = 0.28–0.33$ p.f.u..

The observed biotite-absent peak assemblage $g-ksp-pl-q-ilm(-liq)$ cannot be well predicted in Fig. 8 because orthopyroxene, a common phase in the higher temperatures, is absent in the final assemblage. The measured matrix plagioclase compositions can also suggest temperatures above 1000 °C at 9 kbar, and a subsequent cooling path would not yield regular zoning as observed in sample JD1334. However, the measured X_{An} of 0.43–0.45 in the inclusion plagioclase could yield much higher temperatures of 990–1130 °C from 2–9 kbar (Fig. 8). If taking this into account, there would be two possible P–T paths: path-I dominant of cooling and path-II dominant of increasing pressure at first followed by cooling. The calculated changes in phase modes and compositions (Table 5) suggest that metamorphic evolutions along the both P–T paths would cause growth of garnet in the assemblages above the stability of bitoite, and garnet and orthopyroxene will be consumed in the biotite-bearing assemblages. Metamorphic evolution is dominated by melt crystallization via $opx + ilm + pl + liq = g + ru + q + ksp$ in the modelled peak

assemblage $g\text{-ksp-opx-ru-ilm-pl-q-liq}$, and $g + ilm + ksp + liq = bi + q + pl$ in the final assemblage $g\text{-bi-ksp-ilm-pl-q-liq}$. These metamorphic reactions may have been responsible for the disappearance of orthopyroxene and rutile in the peak assemblage and appearance of biotite in the final assemblage.

The overprinting assemblage in this sample is neglected for its weak development.

Sample JD15126

The P–T pseudosection calculated for sample JD15126 is drawn for plagioclase, quartz and rutile in excess with the P–T window of 2–12 kbar and 700–1200 °C (Fig. 9). The fluid-absent solidus occurs at ~880 °C under 6–12 kbar. The observed final assemblage $g\text{-bi-ksp-pl-q-ru-sill(-liq)}$ defines a P–T range of 7–12 kbar and 880–890 °C. The measured X_{gr} of 0.03–0.05 and X_{An} of 0.34–0.30 define a pressure range of 7.5–10 kbar in the final assemblage, while the measured $X_{py} = 0.37\text{--}0.40$ in garnet and $X_{Mg\text{-}bi}$ in the matrix biotite mostly suggest cooling conditions in the subsolidus fields. The predicted Ti content in biotite is only 0.19 p.f.u. at the biotite-out temperature, significantly lower than the measured values ($Ti = 0.23\text{--}0.29$ p.f.u.).

The observed peak assemblage $g\text{-ksp-pl-q-ru-sill(-liq)}$ without biotite is predicted to define a temperature range of 890–1080 °C under 9.5 kbar. The flat profile with $X_{gr} = 0.04\text{--}0.05$ in the core of type-1 garnet (Figs. 5d, e) seems to suggest a P–T path with decreasing pressure and temperature in between the X_{gr} isopleths of

gr4 and gr5. However, metamorphic evolution along this path will not cause the growth of garnet. Thus, the flat X_{gr} profile could be better attributed to ion diffusion and an isobaric cooling path is inferred under a pressure range of 9–10 kbar. The decreasing of X_{gr} (0.04→0.03) from the narrow rim of type-1 garnet may suggest a P–T vector dominant of pressure decrease (Fig. 9). The core-rim decreasing in X_{An} in the coarse-grained matrix plagioclase may suggest that the growth of plagioclase may have occurred by cooling or pressure increasing in the higher-T assemblages beyond the stability of K-feldspar and sillimanite. The measured core-rim zoning with decreasing X_{An} (0.49→0.47) from plagioclase inclusions in type-1 garnet could yield a much higher temperature or lower pressure assemblages without K-feldspar and sillimanite. Like that for sample JD1453, two possible P–T paths can be inferred as shown in Fig. 9: path-I dominant of cooling and path-II dominant of increasing pressure at first followed by cooling. The calculated changes in phase modes and compositions (Table 5) indicate that metamorphic evolution may result in growth of garnet and plagioclase together with melt crystallization during the early cooling stage of path-I and the pressure-increasing stage of path-II, and metamorphic reactions are modelled to be $pl + liq = g + q + sill + ksp$ in the field of peak assemblage, and $g + ksp + ru + liq = pl + q + sill + bi$ in the field of the final assemblage.

5. Zircon U–Pb dating

Samples JD1334, JD1453 and JD15126 were selected for zircon U–Th–Pb isotopic analyses. The detailed analytical results are listed in Supplementary Table S1.

Thirty five analyses were performed on thirty-four zircon grains for *sample JD1334*. Zircon from this sample exhibits oval to round shapes with lengths ranging from 50–100 μm and length/width ratios of 1:1 to 2:1 (Fig. 10a). Cathodoluminescence images suggest two types of zircon grains: type I showing core-rim structure with blurred oscillatory zoning (e.g. spot #28, 33) or dark structureless characters in the core (e.g. spot #1, 20, 35), and with relatively high luminescence metamorphic growth rims (e.g. spot #21, 29), and type II showing sector zoning (e.g. spot #9). Due to the abnormal signal for analyses #6, #14, #15 and #30, they were excluded from age calculations. The remaining thirty one analyses were divided into three age groups (Fig. 11a). The first group comprises eleven analyses of oscillatory-zoning and/or structureless cores, with apparent $^{207}\text{Pb}/^{206}\text{Pb}$ ages ranging from 2525 ± 8 Ma to 3340 ± 12 Ma and Th/U ratios of 0.23–0.67 (av. 0.49), representing the ages of detrital zircon of magmatic origin. The second group consists of seventeen analyses of metamorphic growth rims and/or sector zoning, with apparent $^{207}\text{Pb}/^{206}\text{Pb}$ ages of 2427 ± 9 Ma to 2507 ± 9 Ma and Th/U ratios of 0.02–0.85 (av. 0.31). These analyses yield a weighted mean $^{207}\text{Pb}/^{206}\text{Pb}$ age of 2478 ± 13 Ma (MSWD = 7.8) in the concordia diagram (Fig. 11a). Spots #20, #02, #01 constitute the third age group and give apparent $^{207}\text{Pb}/^{206}\text{Pb}$ ages of 2388 ± 8 Ma, 2378 ± 8 Ma and 2078 ± 9 Ma with Th/U ratios of 0.04, 0.14 and 0.16, respectively. They plot on the concordia curve and spots #20, #02 define a concordia age of 2382 ± 6 Ma (MSWD = 0.022).

Thirty three U–Pb analyses were performed on thirty-one zircon grains for

Sample JD1453. Zircon in this sample mostly exhibits short prismatic and spherical-oval shapes with a size of 70–150 μm and length/width ratios of 1:1 to 2:1 (Fig. 10b). Most zircon grains are characterized by oscillatory zoned cores (e.g. spot # 19, 20) and metamorphic growth rims (e.g. spot # 2, 23). A few zircon grains display dark or irregular cores (e.g. spot #14, 30), and some grains show sector zoning (e.g. spot # 21). They were divided into three age groups (Fig. 11b). The first group involving twenty-three analyses from oscillatory-zoned cores have apparent $^{207}\text{Pb}/^{206}\text{Pb}$ ages ranging from 2502 ± 13 Ma to 2689 ± 13 Ma and Th/U ratios of 0.12–1.64 (av. 0.61), and plot on or near the concordia curve, except for two analyses (spots #19 and #24) which plot below the curve, indicating effect of Pb-loss. We suggest these oscillatory cores are of magmatic origin. The second group, including six analyses from metamorphic growth rims and grains with sector zoning, have apparent $^{207}\text{Pb}/^{206}\text{Pb}$ ages from 2482 ± 15 Ma to 2509 ± 10 Ma with a weighted mean $^{207}\text{Pb}/^{206}\text{Pb}$ age of 2498 ± 9 Ma (MSWD = 0.69), and relatively low Th/U ratios of 0.04–0.34 (av. 0.11). They plot on the concordia curve, yielding a concordant age of 2497 ± 5 Ma (MSWD = 0.014). The third group involving the remaining four analyses from dark or irregular cores, give much younger apparent $^{207}\text{Pb}/^{206}\text{Pb}$ ages from 2301 ± 13 Ma to 2404 ± 15 Ma with Th/U ratios of 0.48–0.64 (av. 0.56), three of which yield a concordant age of 2401 ± 7 Ma (MSWD = 0.031) with weighted mean $^{207}\text{Pb}/^{206}\text{Pb}$ age of 2400 ± 14 Ma (MSWD = 0.20).

Thirty spots were analyzed on thirty zircon grains for **sample JD15126**, where zircon shows lath and spherical-oval shapes with a size of 50–110 μm , with

length/width ratios of 1:1 to 2:1 (Fig. 10c). Most zircon grains exhibit clear or blurred oscillatory zoning (e.g. spots #1, #10, #18, #6 and #23), and a few grains are relatively homogeneous with low luminescence (e.g. spots #13). Five analyses (spots #7, #12, #14, #26 and #28) are rejected for age calculations, owing to their abnormal signal peaks. The remaining twenty five analyses were divided into two age groups (Fig. 11c). The first group including twenty two analyses from oscillatory zoning exhibits apparent $^{207}\text{Pb}/^{206}\text{Pb}$ ages of 2505 ± 10 Ma to 3585 ± 12 Ma. The second group including three analyses (spots #19, #29 and #13) shows $^{207}\text{Pb}/^{206}\text{Pb}$ ages of 2473 ± 13 Ma, 2478 ± 14 Ma and 2496 ± 12 Ma, and Th/U ratios of 0.02, 0.01 and 0.13, yielding a weighted mean $^{207}\text{Pb}/^{206}\text{Pb}$ age of 2483 ± 15 Ma (MSWD = 0.95) in the concordia diagram (Fig. 11c).

Zircon with the first age group from the three samples have significantly high chondrite-normalized REE values and the heavy rare earth element (HREE) contents are particularly high, showing left-facing slopes on the chondrite-normalized REE plots (Fig. 12), which further prove their magmatic origin. In contrast, zircons with the second group show relatively low total REE, and distinctly low HREE contents, exhibiting flat HREE patterns that could be a result of zircon-garnet coexistence (Rubatto, 2002; Rehman et al., 2016), further supporting their metamorphic origin. Zircon grains with the third age group show variant REE patterns, similar to those of magmatic zircon in sample JD1453, and similar to those of metamorphic zircon in sample JD1334.

6. Discussion and conclusions

6.1 Metamorphic evolution of pelitic granulites

Based on the petrographic characteristics and phase equilibria modelling, four generations of assemblages involving final, peak, inclusion and overprinting stages were identified for pelitic granulites from the eastern Hebei terrane.

P–T conditions of the final assemblages

The observed final assemblages with presence of biotite for the three samples yield similar P–T conditions of 8.0–9.5 kbar/870–890 °C (Figs 6–9), giving an apparent thermal gradient of 25 °C/km (Fig. 13). Although the low–T limits are constrained by the fluid-absent solidi that depend on the H₂O contents (higher H₂O contents yield lower solidus), the right match between the measured and the predicted mineral chemical compositions and modal proportions (Table 5) can provide additional constraints on the P–T conditions of the final assemblages or the location of the solidi. In addition, the locations of mineral composition isopleths in the suprasolidus fields would not be significantly affected by the solidus position. It is noteworthy that the predicted Ti content in biotite is significantly lower than the measured values, suggesting that the temperature of the final assemblages would be somewhat underestimated. The obtained P–T conditions for the final assemblages are in agreement with those of the previous studies for mafic granulites (Chen and Li, 1996; He and Ye, 1992; Zhao et al., 1998).

Isobaric cooling of the peak assemblages

The observed peak assemblages without biotite in samples JD1334 and JD15126

are modelled to be stable in large P–T ranges (Figs. 6, 9). In sample JD1334, the measured core-rim zoning with X_{An} decreasing from coarse-grained plagioclase in the matrix and weakly garnet core-rim zoning with X_{gr} increasing are predicted to be consistent with a cooling path, where the isopleths of maximum X_{An} and minimum X_{gr} from grains cores define a peak P–T condition of ~1050 °C and 9.8 kbar in the field of peak assemblage. In sample JD15126, the flat X_{gr} profiles in the garnet core could be attributed to ion diffusion and is better interpreted to reflect isobaric cooling under 9–10 kbar. The observed peak assemblage in sample JD1453 cannot be well modelled in pseudosection for orthopyroxene is predicted to be common under higher temperatures but consumed through metamorphic reactions during cooling under suprasolidus conditions. However, the flat compositional zoning of garnet and plagioclase in the matrix from sample JD1453 only record the final solidus condition and cannot be well used to constrain a cooling path.

Metamorphic evolution recorded by the plagioclase inclusions

Plagioclase inclusions with high X_{An} in garnet in samples JD1453 and JD15126 are predicted to be stable at much lower-P and/or higher-T fields than the stabilities of the peak assemblages. This suggests two possible P–T paths: an isobaric cooling from > 1100 °C and a path dominant of pressure increasing at first followed by cooling in the P–T fields of the peak assemblages. These two paths are consistent with the measured zoning with core-rim decreasing in X_{An} from both inclusion and the coarse matrix grain of plagioclase in sample JD15126 (Fig. 9). It should be noted that there are considerable uncertainties for the phase modelling results in the fields

beyond the stability of peak assemblages due to the uncertainty of water contents. The water contents used for calculating the pseudosections were determined on the basis of the stability of the final assemblages. If the rocks contain lower water contents at their peak stages, the predicted differences in phase equilibria from those shown in Figs 6–9 are that the stability fields of K-feldspar and sillimanite will be enlarged and the amount of melt will decrease (White et al., 2001; Wei, 2016), which will result in considerable changes in phase topology. The low water contents in pelitic granulites may have been attributed to melt loss during prograde metamorphic evolution (White et al. 2001, 2002). However, the bulk rock compositions of the concerned samples are distinct from the UHT granulites that have experienced a large amount of melt loss with high $Mg^{\#} = 70\text{--}80$ and low content of Na_2O and CaO (e.g. Kelsey et al., 2004). That is to say, there would not be a lot of melt lost from the studied samples. In addition, phase modelling of zircon growth or dissolution in melt-bearing system implies that zircon in high-grade rocks tends to be dissolved in melt (Kelsey and Powell, 2011). The presence of numerous detrital zircons also suggests lack of abundant melt in the peak stage, or at least, much less than the modelled values in Table 5.

There is one possibility for a pelitic rock to have low melt (or water) contents under granulite facies is that the rock underwent heating under low pressures. For example, if a rock was heated under low pressures along a P–T path as shown in Fig. 13, the rock will be dehydrated through decomposition of hydrous phases, such as muscovite and biotite under subsolidus conditions, and there still be very small

amount of melt formed when the P–T path meets the dry solidus of granodiorite, i.e. at 1010 °C/3 kbar. However, the X_{An} isopleths in plagioclase inclusions are plotted above the dry solidus. Phase modelling suggests that their locations will move to higher temperatures with decreasing H₂O contents, and the resulting melt mode will be very high even under dry conditions. Thus, we cannot rule out a possibility that the Ca-rich plagioclase inclusions in garnet may not represent the equilibrium metamorphic evolution as modelled in Figs. 8, 9, but represent local equilibrium conditions because of the fast moving of rocks or lack of fluids. As a consequence, the X_{An} isopleths of the plagioclase inclusion are not relied too much for constructing the P–T paths of the granulites, and the P–T paths are inferred to proceed under temperatures below the dry solidus in Fig. 13.

Although there are considerable uncertainties in the locations of the plagioclase X_{An} isopleths in the fields beyond the stabilities of the peak assemblages, they do suggest a possibility that the concerned rocks may have experienced UHT metamorphic stages with temperature much higher than that recorded by their final assemblages. This can be supported by the following lines of evidence:

(i) The measured Ti in biotite ranging from 0.27–0.33 p.f.u. is much higher than the modelled values on the biotite-out, suggesting the Ti-rich phase could be stable to higher temperatures if the stability fields of biotite could be enlarged by incorporating components, i.e. fluorine (e.g. Hensen and Osanai, 1994). Biotite from the Zhaojiayao granulites in the Khondalite belt of North China Craton shows similar Ti contents to those in our samples, which were estimated to be stable > 1000 °C (Li and Wei, 2016).

Moreover, experimental work of Stevens et al. (1997) suggests that the upper limits of Ti-biotite in the pelites and greywackes are $> 950\text{ }^{\circ}\text{C}$ at 9 kbar (Fig. 13), where biotite contains Ti up to 0.25 p.f.u., lower than the Ti contents in the concerned samples. Thus, the final assemblages with Ti-rich biotite could be stable to higher temperatures than the modelled values, and the peak assemblages without biotite could represent UHT conditions greater than $950\text{ }^{\circ}\text{C}$.

(ii) The pelitic granulites coexist with two pyroxene granulites and charnockites.

The two pyroxene granulites are dominated by anhydrous minerals with variant amounts of amphibole where amphibole was observed to be retrograde phase by Chen and Li (1996). Although these mafic granulites were estimated to show peak temperatures of $866\text{--}922\text{ }^{\circ}\text{C}$ by Chen and Li (1996) using conventional thermometers, they may suggest much higher temperature conditions according to experimental results that the disappearance of amphibole in mafic rocks mostly occurs in $1000\text{--}1100\text{ }^{\circ}\text{C}$ (e.g. Moyen and Stevens, 2006, Fig. 13).

As a summary, the final, peak and inclusion assemblages in the pelitic granulites suggest an anti-clockwise P–T path involving early-stage heating under low pressures, followed by pressure-increasing to the P–T fields of the peak assemblages, and subsequent cooling to the P–T fields of the final assemblages. It is worthy noting that a P–T vector dominant of pressure-decreasing can be inferred from the decreasing X_{gr} in the narrow rim section of garnet in sample JD15126, indicating decompression under subsolidus conditions (Figs 9, 13).

Metamorphic evolution recorded by the overprinting assemblages

The pelitic granulites were differently overprinted by the assemblage characteristic of formation of garnet coronae or outer rims around garnet, together with the formation of tiny grains of plagioclase, K-feldspar, biotite and quartz etc. in local domains. A case study from sample JD1334 suggests that the P–T conditions of the overprinting assemblage are 10–12 kbar and 830–880 °C (Fig. 7). Chen and Li (1996) observed that these overprinting textures were developed in various granulites and mafic dykes and inferred that they were Paleoproterozoic products on the basis of field geological context. Duan et al. (2015) reported that the mafic dykes have experienced high-pressure granulite-facies metamorphism characteristic of clockwise P–T paths with peak conditions of 11–13 kbar/790–810 °C and post-peak cooling ages of ~1.82 Ga. The peak P–T conditions from the metabasic dykes are similar to that estimated for the overprinting assemblage in sample JD1334 (Fig. 13), suggesting they were the products of a same metamorphic event of high-pressure granulite-facies in the Paleoproterozoic era. The Paleoproterozoic granulites show lower peak temperature and higher peak pressure than those of the granulites of early stages.

6.2 Zircon U–Pb data of pelitic granulites

Zircon age dating for three pelitic granulites yields wide range of apparent $^{207}\text{Pb}/^{206}\text{Pb}$ ages from 3.5 Ga to 2.1 Ga, which are divided into three groups. The first age group from 3.5 Ga to 2.5 Ga with a peak at 2.6–2.5 Ga is obtained from zircon grains characterized by oscillatory zoned cores and high HREE contents with left-facing slopes on the chondrite-normalized REE plots, indicative of their

magmatic origin. The peak ages of 2.6–2.5 Ga are consistent with the abundant magmatic precursors of TTG gneisses in eastern Hebei (e.g. Geng et al., 2006, 2010; Yang et al., 2008; Nutman et al., 2011; Wan et al., 2012; Zhang et al., 2012; Guo et al., 2013, 2015; Bai et al., 2014, 2015). The youngest detrital zircon age peak of ~2.5 Ga in this group is interpreted as the sedimentary deposition time of the pelitic granulites. In addition, the older $^{207}\text{Pb}/^{206}\text{Pb}$ ages from 3.5 Ga to 2.7 Ga of detrital zircon in the group are consistent with those reported for eastern Hebei (e.g. Jahn et al., 1987; Liu et al., 1992; Nutman et al., 2011, 2014).

The second age group with a weighted mean $^{207}\text{Pb}/^{206}\text{Pb}$ age of ~2.48 Ga is obtained from zircon grains with metamorphic growth rims, sector zoning and low HREE contents with flat HREE patterns, suggesting their metamorphic origin. Accordingly, the 2.48 Ga is thought to be the metamorphic age of the first phase of pelitic granulites coeval with the time of regional granulite-facies metamorphism revealed in the previous studies for mafic granulites, TTG gneisses and charnockites (e.g. Zhao et al., 1998; Geng et al., 2006; Nutman et al., 2011; Yang et al., 2015). Phase equilibria modelling in the ZrO_2 -bearing system suggests that in melt-bearing high-grade metamorphic rocks zircon tends to be dissolved in melt and newly grown zircon should record the age of melt crystallization during cooling (Kelsey and Powell, 2011; Zhang et al., 2013). Accordingly, the age of 2.48 Ga could be interpreted to represent uplifting and cooling ages of granulite terranes (Fig. 13).

The third age group of $^{207}\text{Pb}/^{206}\text{Pb}$ ages from 2.4–2.1 Ga is obtained from zircon grains with irregular character, and/or blurred oscillatory zoning and shows both

magmatic and metamorphic zircon REE pattern character, which was considered to be complex or unknown origin. As there are only a few data in this group, it is hard to interpret their real geological meanings (e.g. Guo et al., 2013, 2015; Bai et al., 2014, 2015).

6.3 Tectonic implications

As mentioned above, the Archean supracrustal rocks of granulite-facies commonly occur as localized slivers or rafts in vast oceans of granitoids, and there is a tendency that the higher the metamorphic grades the smaller the scales of the supracrustal slivers or rafts. The anticlockwise P–T paths that involve heating, pressure-increasing, cooling and uplifting stages recovered from the pelitic granulites in this study suggest a tectonic scenario to explain the particular occurrence of the Archean supracrustal granulites. Firstly, supracrustal sediments experienced thermal event under low pressures attributed to the intrusion of high-temperature TTGs, resulting in dehydrations of hydrous phases like muscovite and biotite under subsolidus conditions (Fig.13). Then, the dried metasediments, potentially denser than the surrounding lithologies tend to drop into the TTG magma ocean, causing the pressure-increase in the metasediments. As the metasediments dehydrated, they could skip intensive melting due to their fast dropping thus could prevent metamorphic reequilibration even their P–T path could meet the dry solidus. Actually, as almost every supracrustal sliver is interlayered with iron formations in the Taipingzhai region, it could be expected that the metasediments dropped following the dense iron-bearing

rocks. Thirdly, the dropped metasediments experienced cooling under crustal level of ~35 km for the case we concerned in coupled with the crystallization of the surrounding TTG magma to form the observed final assemblages. Finally, they uplifted as a consequence of the doming processes in Archean terranes (Campbell and Hill, 1988; Collins et al., 1998; Parmenter et al., 2006; Lin and Beakhouse, 2013). It could be postulated that the lower-metamorphic grade greenschist belts represent their shallow dropping into magma oceans, and some supracrustal blocks of amphibolite-facies represent their deeper positions. Zircon U–Pb data suggest that the deposition age of pelitic granulites from eastern Hebei was ~2.5 Ga, and the metamorphic age was ~2.48 Ga, indicating that the heating, dropping and cooling processes occurred in an time interval of ~20 My.

Acknowledgements

Special thanks are due to Editor in Chief Prof. Guochun Zhao, Prof. Chunming Wu and an anonymous reviewer for their constructive comments and improving the manuscript. This work was financially supported by the National Natural Science Foundation of China (Grant Number 41430207). We thank Hong Qin, Fang Ma, Guiming Shu and Xiaoli Li for their help in experimental analyses, and Jiahui Qian, Zhuang Li and Chao Wang for their involvement in the field work.

References

Bai, X., Liu, S.W., Guo, R.R., Zhang, L.F., Wang, W., 2014. Zircon U–Pb–Hf isotopes and

- geochemistry of Neoproterozoic dioritic–trondhjemitic gneisses, Eastern Hebei, North China Craton: constraints on Petrogenesis and tectonic implications. *Precambrian Res.* 251, 1–20.
- Bai, X., Liu, S.W., Guo, R.R., Wang, W., 2015. Zircon U–Pb–Hf isotopes and geochemistry of two contrasting Neoproterozoic charnockitic rock series in Eastern Hebei, North China Craton: Implications for petrogenesis and tectonic setting. *Precambrian Res.* 267, 72–93.
- Bleeker, W., 2002. Archean tectonics: a review, with illustrations from the Slave Craton. In: Fowler, C.M.R., Ebinger, C.J., Hawkesworth, C.J. (Eds.). *The Early Earth: Physical, Chemical and Biological Development*, 199. Geological Society [London] Special Publication, pp. 151–181.
- Boniface, N., Mruma, A.H., 2012. Structural analysis, metamorphism, and geochemistry of the Archean granitoids–greenstones of the Sukumaland Greenstone Belt around Geita Hills, Northern Tanzania. *Natural Science* 4(8), 526–535.
- Brown, M., 2007. Metamorphic conditions in orogenic belts: a record of secular change. *International Geology Review* 49, 193–234.
- Campbell, I. H., Hill, R. I., 1988. A two–stage model for the formation of the granite ± greenstone terrains of the Kalgoorlie–Norseman area, Western Australia. *Earth and Planetary Science Letters* 90, 11–25.
- Carson, C.J., Powell, R., Clarke, G.L., 1999. Calculated mineral equilibria for eclogites in CaO–Na₂O–FeO–MgO–Al₂O₃–SiO₂–H₂O: application to the Pouébo Terrane, Pam Peninsula, New Caledonia. *J. Metamorphic Geol.* 17, 9–24.
- Chen, M.Y., 1990. Metabasic dyke swarms in a high-grade metamorphic terrane: a case study in the Taipingzhai–Jinchangyu area, Eastern Hebei Province. *Acta Geol. Sin.* 2, 157–169 (in

Chinese with English abstract).

- Chen, M.Y., Li, S.X., 1996. The evolution of granulite facies metamorphism in eastern Hebei province. *Acta Petrol. Sin.* 2, 343–357 (in Chinese with English abstract).
- Collins, W.J., Van Kranendonk, M.J., Teyssier, C., 1998. Partial convective overturn of Archaean crust in the East Pilbara Craton, Western Australia; driving mechanisms and tectonic implications. *J. Structural Geol.* 20, 1405–1424.
- Condie, K. C., 1981. Archean Greenstone Belts. *Earth-Science Reviews* 18(1), 95–96.
- Duan, Z.Z., Wei, C.J., Qian, J.H., 2015. Metamorphic P-T paths and Zircon U–Pb age data for the Paleoproterozoic metabasic dykes of high-pressure granulite facies from Eastern Hebei, North China Craton. *Precambrian Res.* 271, 295–310.
- Frost, B.R., Chacko T., 1989. The Granulite Uncertainty Principle: Limitations on Thermobarometry in Granulites. *Journal of Geol.* 97(4), 435–450.
- Geng, Y.S., 1998. Basic volcanic events and evolution of early Precambrian in the Eastern Hebei province. In: *Essays of Early Precambrian Geological Research in the North China Craton.* Geol. Publ. House, Beijing, pp. 105–122 (in Chinese).
- Geng, Y.S., Liu, F.L., Yang, C.H., 2006. Magmatic event at the end of the Archean in Eastern Hebei Province and its geological implication. *Acta Geol. Sin. (English Edition)* 80, 819–833.
- Geng, Y.S., Shen, Q.H., Ren, L.D., 2010. Late Neoproterozoic to Early Paleoproterozoic magmatic events and tectonothermal systems in the North China Craton. *Acta Petrol. Sin.* 26, 1945–1966.
- Geng, Y.S., Du, L.L., Ren, L.D., 2012. Growth and reworking of the early Precambrian

- continental crustal in the North China Craton: constraints from zircon Hf isotopes. *Gondwana Res.* 21, 517–529.
- Ghosh, J.G., Wit, M. J., Zartman, R.E., 2004. Age and tectonic evolution of Neoproterozoic ductile shear zones in the Southern Granulite Terrain of India, with implications for Gondwana studies, *Tectonics* 23(3), 297–319.
- Guo, R.R., Liu, S.W., Santosh, M., Li, Q.G., Bai, X., Wang, W., 2013. Geochemistry, zircon U–Pb geochronology and Lu–Hf isotopes of metavolcanics from eastern Hebei reveal Neoproterozoic subduction tectonics in the North China Craton. *Gondwana Res.* 24, 664–686.
- Guo, R.R., Liu, S.W., Wyman, D., Bai, X., Wang, W., Yan, M., Li, Q.G., 2015. Neoproterozoic subduction: a case study of arc volcanic rocks in Qinglong–Zhuzhangzi area of the Eastern Hebei Province, North China Craton. *Precambrian Res.* 264, 36–62.
- Harley, S.L., 1989. The origins of granulites: a metamorphic perspective. *Geological Magazine* 126, 215–247.
- Hensen, B.J., Osanai, Y., 1994. Experimental study of dehydration melting of F-bearing biotite in model pelitic compositions. *Mineralogical Magazine* 58A, 410–411.
- He, G. P., Ye, H.W., 1992. The evolution of metamorphism in granulite facies terrane, Eastern Hebei Province. *Acta Petrol. Sin.* 8, 129–135 (in Chinese with English abstract).
- Holland, T.J.B., Powell, R., 1998. An internally consistent thermodynamic data set for phases of petrological interest. *J. Metamorphic Geol.* 16, 309–343.
- Holland, T.J.B., Powell, R., 2003. Activity–composition relations for phases in petrological calculations: an asymmetric multicomponent formulation. *Contrib. Mineral. Petrol.* 145, 492–501.

- Jahn, B.M., Auvray, B., Cornichet, J., Bai, Y.L., Shen, Q.H., 1987. 3.5 Ga old amphibolites from eastern Hebei Province, China: Field occurrence, petrography, Sm–Nd isochron age and REE geochemistry. *Precambrian Res.* 34, 311–346.
- Käyaho, A., Hölttä, P., Whitehouse, M., 2007. U–Pb zircon geochronology of selected Neoproterozoic migmatites in eastern Finland: *Bulletin of the Geological Society of Finland*, v. 79(1), pp. 95–115.
- Kelsey, D.E., White, R.W., Powell, R., Wilson, C.J.L., Quinn, C.D., 2003. New constraints on metamorphism in the Rauer Group, Prydz Bay, east Antarctica. *J. Metamorphic Geol.* 21, 739–759.
- Kelsey, D.E., White, R.W., Holland, T.J.B., Powell, R., 2004. Calculated phase equilibria in K_2O – MgO – FeO – Al_2O_3 – SiO_2 – H_2O for sapphirine–quartz-bearing mineral assemblages. *J. Metamorphic Geol.* 22, 559–578.
- Kelsey, D.E., Powell, R., 2011. Progress in linking accessory mineral growth and breakdown to major mineral evolution in metamorphic rocks: a thermodynamic approach in the Na_2O – CaO – K_2O – FeO – MgO – Al_2O_3 – SiO_2 – H_2O – TiO_2 – ZrO_2 system. *J. Metamorphic Geol.* 29, 151–166.
- Korhonen, F.J., Brown, M., Clark, C., Bhattacharya, S., 2013. Osumilite–melt interactions in ultrahigh temperature granulites: phase equilibria modelling and implications for the P–T–t evolution of the Eastern Ghats Province, India. *J. Metamorphic Geol.* 31, 881–907.
- Kröner A., 1984. Evolution, growth and stabilization of the Precambrian lithosphere. *Physics and Chemistry of the Earth* 15(84), 69–106.
- Kwan, L.C.J., Zhao, G.C., Yin, C.Q., Geng, H.Y., 2016. Metamorphic P–T path of mafic granulites

- from Eastern Hebei: Implications for the Neoproterozoic tectonics of the Eastern Block, North China Craton. *Gondwana Res.* 37, 20–38.
- Li, T.S., Zhai, M.G., Peng, P., Chen, L., Guo, J.H., 2010. Ca. 2.5 billion year old coeval ultramafic–mafic and syenitic dykes in Eastern Hebei: implications for cratonization of the North China Craton. *Precambrian Res.* 180, 143–155.
- Li, X.W., Wei, C.J., 2016. Phase equilibria modelling and zircon age dating of pelitic granulites in Zhaojiayao, from the Jining Group of the Khondalite Belt, North China Craton. *J. Metamorphic Geol.* 34, 595–615.
- Lin, S.F., Beakhouse, G.P., 2013. Synchronous vertical and horizontal tectonism at latest ages of Archean cratonization and genesis of Hemlo gold deposit, Superior craton, Ontario, Canada. *Geology* 41, 359–362.
- Liu, C.H., Zhao, G.C., Liu, F.L., Shi, J.R., 2014. Zircon U–Pb and Lu–Hf isotopic and whole–rock geochemical constraints on the provenance and age of the Shuangshanzi and Qinglonghe Groups in Eastern Hebei: Implications for the tectonic evolution of the Eastern Block. *Precambrian Res.* 255, 699–715.
- Liu, D.Y., Nutman, A.P., Compston, W., Wu, J.S., Shen, Q.H., 1992. Remnants of ≥ 3800 Ma crust in the Chinese part of the Sino–Korean craton. *Geology* 20, 339–342.
- Liu, D.Y., Wan, Y.S., Wu, J.S., Wilde, S.A., Zhou, H.Y., Dong, C.Y., Yin, X.Y., 2007. Eoarchean rocks and zircons in the North China Craton. In: van Kranendonk, M., Smithies, R.H., Bennett, V. (Eds.), *Earth's Oldest Rocks*, 15, Amsterdam, The Netherlands, Elsevier Series Developments in Precambrian Geology, pp. 251–273.
- Liu, D.Y., Wilde, S.A., Wan, Y.S., Wu, J.S., Zhou, H.Y., Dong, C.Y., Yin, X.Y., 2008. New U–Pb

- and Hf isotopic data confirm Anshan as the oldest preserved segment of the North China Craton. *Am. J. Sci.* 308, 200–231.
- Liu, S.W., Zhang, J., Li, Q.G., Zhang, L.F., Wang, W., Yang, P.T., 2012. Geochemistry and U–Pb zircon ages of metamorphic volcanic rocks of the Paleoproterozoic Lvliang Complex and constraints on the evolution of the Trans–North China Orogen, North China Craton. *Precambrian Res.* 222–223, 173–190.
- Lü, B., Zhai, M.G., Li, T.S., Peng, P., 2012. Zircon U–Pb ages and geochemistry of the Qinglong volcano–sedimentary rock series in Eastern Hebei: Implication for 2500 Ma intra–continental rifting in the North China. *Precambrian Res.* 208–211, 145–160.
- Moyen, J.F., Stevens, G., 2006. Experimental constraints on TTG petrogenesis: Implications for Archean geodynamics. *American Geophysical Union* 164, 149–175.
- Nutman, A.P., Wan, Y.S., Du, L.L., Friend, C.R.L., Dong, C.Y., Xie, H.Q., Wang, W., Sun, H.Y., Liu, D.Y., 2011. Multistage late Neoproterozoic crustal evolution of the North China Craton, Eastern Hebei. *Precambrian Res.* 189, 43–65.
- Nutman, A.P., Maciejowski, R., Wan, Y.S., 2014. Protoliths of enigmatic Archean gneisses established from zircon inclusion studies: case study of the Caozhuang quartzite, E., Hebei, China. *Geosci. Frontiers* 5(4), 445–455.
- Parmenter, A.C., Lin, S., Corkery, M.T., 2006. Structural evolution of the Cross Lake greenstone belt in the northwestern Superior Province, Manitoba: implications for relationship between vertical and horizontal tectonism. *Canadian Journal of Earth Sciences* 43, 767–787.
- Pattison, D.R.M., Chacko, T., Farquhar, J., McFarlane, C.R.M., 2003. Temperatures of granulite

- facies metamorphism: constraints from experimental phase equilibria and thermobarometry corrected for retrograde exchange. *Journal of Petrology* 44, 867–900.
- Peucat, J.J., Mahabaleswar, B., Jayananda, M., 1993. Age of younger tonalitic magmatism and granulitic metamorphism in the South Indian transition zone (Krishnagiri area): Comparison with older Peninsular gneisses from the Gorur–Hassan area, *J. Metamorphic. Geol.* 11, 879–888.
- Powell, R., Holland, T.J.B., 2008. On thermobarometry. *J. Metamorphic Geol.* 26, 155–179.
- Qian, X.L., Cui, W.Y., Wang, S.Q., Wang, G.Y., 1985. *Geology of Precambrian Iron Ores in Eastern Hebei Province, China*. Hebei Science and Technology Press, Shijiazhuang (in Chinese).
- Rehman, H. U., Lee, H-Y., Chung, S-L., Khan, T., O'Brien, P. J., Yamamoto, H., 2016. Source and mode of the Permian Panjal Trap magmatism: Evidence from zircon U-Pb and Hf isotopes and trace element data from the Himalayan ultrahigh-pressure rocks. *Lithos* 260, 286–299.
- Riciputi, L., Valley, J.W., Mcgregor, V.R., 1990. Conditions of Archaean granulite metamorphism in the Godthab–FisKenaesset region, southern West Greenland. *Journal of Geol.* 8, 171–190.
- Robertson, J.K., Wyllie, P.J., 1971. Experimental Studies on Rocks from the Deboullie Stock, Northern Maine, Including Melting Relations in the Water-deficient Environment. *Journal of Geol.* 79, 549–571.
- Rubatto, D., 2002. Zircon trace element geochemistry: partitioning with garnet and the link between U–Pb ages and metamorphism. *Chemical Geol.* 184, 123–138.
- Santosh, M., Liu, S.J., Tsunogae, T., Li, J.H., 2012. Paleoproterozoic ultrahigh temperature granulites in the North China Craton: implications for tectonic models on extreme crustal

- metamorphism. *Precambrian Res.* 222, 77–106.
- Song, B., Nutman, A.P., Liu, D.Y., Wu, J.S., 1996. 3800–2500 Ma crustal evolution in the Anshan area of Liaoning Province, northeastern China. *Precambrian Res.* 78, 79–94.
- Song, S.G., 1990. Metamorphosed basic and ultrabasic dyke swarms in Taipingzhai region, East Hebei. *J. Changchun Univ. Earth Sci.* 20, 421–428 (in Chinese with English abstract).
- Spear, F.S., Cheney, J.T., 1989. A petrogenetic grid for pelitic schists in the system $\text{SiO}_2\text{--Al}_2\text{O}_3\text{--FeO--MgO--K}_2\text{O--H}_2\text{O}$. *Contrib. Mineral. Petrol.* 101, 149–164.
- Stevens, G., Clemens, J.D., Droop, G.T.R., 1997. Melt production during granulite facies anatexis: experimental data from “primitive” metasedimentary protoliths. *Contrib. Mineral. Petrol.* 128, 352–370.
- Sun, D.Z., 1984. *The Early Precambrian Geology of the Eastern Hebei*. Tianjin Science and Technology Press, Tianjin (in Chinese with English abstract).
- Sun, H.Y., Dong, C.Y., Xie, H.Q., Wang, W., Ma, M.Z., Liu, D.Y., Nutman, A., Wan, Y.S., 2010. *Geol. Rev.* 56, 888–898 (in Chinese with English abstract).
- Sun, S.S., McDonough, W.F., 1989. Chemical and isotopic systematics of oceanic basalts: implications for mantle composition and processes. In: Saunders, A.D., Norry, M.J. (Eds.), *Magmatism in the Ocean Basins: Geological Society London Special Publication*, 42, pp. 313–345.
- Wan, Y.S., Dong, C.Y., Liu, D.Y., Kroner, A., Yang, C.H., Wang, W., Du, L.L., Xie, H.Q., Ma, M.Z., 2012. Zircon ages and geochemistry of late Neoproterozoic syenogranites in the North China Craton: a review. *Precambrian Res.* 222–223, 265–289.
- Wei, C.J., Qian, J.H., Zhou, X.W., 2014. Paleoproterozoic crustal evolution of the

- Hengshan–Wutai–Fuping region, North China Craton. *Geosci. Frontiers* 5, 485–497.
- Wei, C.J., 2016. Granulite facies metamorphism and petrogenesis of granite (II): Quantitative modeling of the HT-UHT phase equilibria for metapelites and the petrogenesis of S-type granite. *Acta Petrol. Sin.* 32(6), 1625–1643.
- White, R.W., Powell, R., Holland, T.J.B., Worley, B.A., 2000. The effect of TiO_2 and Fe_2O_3 on metapelitic assemblages at greenschist and amphibolite facies conditions: mineral equilibria calculations in the system $\text{K}_2\text{O}\text{--}\text{FeO}\text{--}\text{MgO}\text{--}\text{Al}_2\text{O}_3\text{--}\text{SiO}_2\text{--}\text{H}_2\text{O}\text{--}\text{TiO}_2\text{--}\text{Fe}_2\text{O}_3$. *J. Metamorphic Geol.* 18, 497–511.
- White, R.W., Powell, R., Holland, T.J.B., 2001. Calculation of partial melting equilibria in the system $\text{Na}_2\text{O}\text{--}\text{CaO}\text{--}\text{K}_2\text{O}\text{--}\text{FeO}\text{--}\text{MgO}\text{--}\text{Al}_2\text{O}_3\text{--}\text{SiO}_2\text{--}\text{H}_2\text{O}$ (NCKFMASH). *J. Metamorphic Geol.* 19(2), 139–153.
- White, R.W., Powell, R., 2002. Melt loss and the preservation of granulite facies mineral assemblages. *J. Metamorphic Geol.* 20, 621–632.
- White, R.W., Powell, R., Clarke, G.L., 2002. The interpretation of reaction textures in Fe-rich metapelitic granulites of the Musgrave Block, central Australia: constraints from mineral equilibria calculations in the system $\text{K}_2\text{O}\text{--}\text{FeO}\text{--}\text{MgO}\text{--}\text{Al}_2\text{O}_3\text{--}\text{SiO}_2\text{--}\text{H}_2\text{O}\text{--}\text{TiO}_2\text{--}\text{Fe}_2\text{O}_3$. *J. Metamorphic Geol.* 20, 41–55.
- White, R.W., Pomroy, N.E., Powell, R., 2005. An in situ metatexite–diatexite transition in upper amphibolite facies rocks from Broken Hill, Australia. *J. Metamorphic Geol.* 23, 579–602.
- White, R.W., Powell, R., Holland, T.J.B., 2007. Progress relating to calculation of partial melting equilibria for metapelites. *J. Metamorphic Geol.* 25, 511–527.
- Wilde, S.A., Zhao, G.C., Sun, M., 2002. Development of the North China Craton during the Late

- Archean and its amalgamation along a major 1.8 Ga collision zone; including speculations on its position within a global Paleoproterozoic Super-continent. *Gondwana Res.* 5, 85–94.
- Wilde, S.A., Cawood, P.A., Wang, K.Y., Nemchin, A.A., 2005. Granitoid evolution in the Late Archean Wutai Complex, North China Craton. *J. Asian Earth Sci.* 24, 597–613.
- Wilde, S.A., Valley, J.W., Kita, N.T., Cavosie, A.J., Liu, D.Y., 2008. SHRIMP U–Pb and CAMECA 1280 oxygen isotope results from ancient detrital zircons in the Caozhuang quartzite, Eastern Hebei, North China Craton: evidence for crustal reworking 3.8 Ga ago. *Am. J. Sci.* 308, 185–199.
- Wu, J.S., Geng, Y.S., Shen, Q.H., Wan, Y.S., Liu, D.Y., Song, B., 1998. Archean Geology Characteristics and Tectonic Evolution of Sino-Korea Paleo-continent. Geol. Publ. House, Beijing, pp. 212 (in Chinese).
- Yang, J.H., Wu, F.Y., Wilde, S.A., Zhao, G.C., 2008. Petrogenesis and geodynamics of Late Archean magmatism in eastern Hebei, eastern North China Craton: geochronological, geochemical and Nd–Hf isotopic evidence. *Precambrian Res.* 167, 125–149.
- Yang, Q.Y., Santosh, M., Tsunogae, T., 2015. High-grade metamorphism during Archean–Paleoproterozoic transition associated with microblock amalgamation in the North China Craton: Mineral phase equilibria and zircon geochronology. *Lithos*, in press. doi:10.1016/j.lithos.2015.11.018.
- Zhai, M.G., Liu, W.J., 2001. An oblique cross-section of Precambrian crust in the North China Craton. *Phys. Chem. Earth A* 26, 781–792.
- Zhai, M.G., 2011. Cratonization and the Ancient North China continent: a summary and review. *Sci. China Ser. D: Earth Sci.* 54, 1110–1120.

Zhang, L.C., Zhai, M.G., Zhang, X.J., Xiang, P., Dai, Y.P., Wang, C.L., Pirajno, F., 2012.

Formation age and tectonic setting of the Shirengou Neoproterozoic banded iron deposit in eastern Hebei Province: constraints from geochemistry and SIMS zircon U–Pb dating.

Precambrian Res. 222–223, 325–338.

Zhang, Y.H., Wei, C.J., Tian, W., Zhou, X.W., 2013. Reinterpretation of metamorphic age of the

Hengshan Complex, North China Craton. *Chin. Sci. Bull.* 58, 4300–4307.

Zhao, G.C., Wilde, S.A., Cawood, P.A., Lu, L.Z., 1998. Thermal evolution of Archean basement rocks from the eastern part of the North China Craton and its bearing on tectonic setting.

International Geology Review 40, 706–721.

Zhao, G.C., Wilde, S.A., Cawood, P.A., Sun, M., 2001. Archean blocks and their boundaries in the

North China Craton: lithological, geochemical, structural and P–T path constraints and

tectonic evolution. *Precambrian Res.* 107, 45–73.

Zhao, G.C., Sun, M., Wilde, S.A., Li, S.Z., 2005. Late Archean to Paleoproterozoic evolution of

the North China Craton: key issues revisited. *Precambrian Res.* 136, 177–202.

Zhao, G.C., Cawood, P.A., Li, S.Z., Wilde, S.A., Sun, M., Zhang, J., He, Y.H., Yin, C.Q., 2012.

Amalgamation of the North China Craton: key issues and discussion. *Precambrian Res.* 222, 55–76.

Zhao, G.C., Zhai, M.G., 2013. Lithotectonic elements of Precambrian basement in the North China

Craton: Review and tectonic implications. *Gondwana Res.* 23, 1207–1240.

Figure captions

Fig.1 (a) Tectonic subdivision of the North China Craton (NCC) (after Zhao et al.,

2005, 2012). Abbreviations for metamorphic complexes: JP, Jianping; MY, Miyun; EH, Eastern Hebei; CD, Chengde; NH, Northern Hebei; XH, Xuanhua; HA, Huai'an; FP, Fuping; HS, Hengshan; WT, Wutai; LL, Lüliang; ZH, Zanhuang; GY, Guyang; JN-Jining; WD, Wulashan-Daqingshan. (b) Geological map of the Eastern Hebei (modified after Wu et al., 1998; Geng et al., 2006). I. Zunhua high-grade meta-greenstone belt; II. Taipingzhai granulite facies unit; III. Qian'an gneiss dome; IV. Luanxian amphibolite-facies metamorphic belt; V. Qinglong amphibolite–greenschist-facies metamorphic belt.

Fig.2 A geological map of eastern Hebei showing distribution of pelitic granulites.

Fig.3 Field and micrographs of representative pelitic granulite samples from eastern Hebei. (a) A field photo showing the interbedded relationship of pelitic granulites and magnetite quartzite. (b) Partial melting of pelitic granulites. (c) Ca map showing low Ca in the core increasing to high Ca towards inner rim (g_1), overgrown by high Ca outer rim (g_2) from sample JD1334. The red end of the colour spectrum represents high concentrations and the blue-black end represents low concentrations. (d) Anhedral medium- to coarse-grained plagioclase in sample JD1334 (crossed polars). (e) Anhedral fine-grained plagioclase, biotite, quartz and K-feldspar aggregates in sample JD1334. (f) Subhedral coarse-grained garnet porphyroblast (g_1) surrounded by tiny crystal garnet (g_2). The mineral abbreviations are as follows: bi – biotite; g – garnet; ilm – ilmenite; mt – magnetite; ksp – K-feldspar; pl – plagioclase; q – quartz;

opx – orthopyroxene.

Fig. 4 (a) Ca map showing high Ca in the plagioclase inclusion-rich core decreasing to low Ca at rim from sample JD1453. (b) Garnet porphyroblast without plagioclase inclusions from JD1453. (c) Coarse-grained plagioclase in sample JD1453 (crossed polars). (d) Ca map showing high Ca in the plagioclase inclusion-rich core decreasing to low Ca at rim from sample JD15126. (e) Garnet porphyroblast without plagioclase inclusions from JD15126. (f) Anhedral medium- to coarse-grained plagioclase in sample JD15126 (crossed polars). Abbreviations: sill – sillimanite; others are the same as those in Fig. 3.

Fig. 5 Compositional zoning profiles of X_{alm} ($=Fe^{2+}/(Fe^{2+} + Mn + Mg + Ca)$), X_{sps} , X_{py} and X_{gr} defined accordingly across garnet grains from the representative samples JD1334 (a), JD1453 (b, c) and JD15126 (d, e). (f) Compositional zoning of plagioclase characterized by decreasing X_{An} [$= Ca / (Ca + Na + K)$] from core to rim in sample JD1334. (g) Zoning profiles of X_{An} of plagioclase in the matrix (g1) and plagioclase inclusions in garnet (g2) from sample JD1453. (h) Decreasing X_{An} from core to rim of plagioclase in the matrix (h1) and plagioclase inclusions (h2) in garnet grain from sample JD15126. Labels of A, B, g₁ and g₂ correspond to those in Figs. 3–4.

Fig.6 Calculated P–T pseudosection for sample JD1334 in the system

NCKFMASHTO (+ ksp + pl + q + ilm). The pseudosection is presented with isopleths of X_{py} , X_{gr} in garnet, X_{Mg-bi} in biotite, X_{Mg-opx} in orthopyroxene and X_{An} in plagioclase for relevant assemblages. Mineral abbreviations: cd – cordierite; ky – kyanite; liq – silicate liquid/melt; sp – spinel; ru – rutile; other abbreviations are the same as those in Figs. 3–4. Compositions used for modelling are listed in Table 2. The circles with the labels P, A and B are corresponding to those in Table 5.

Fig.7 Calculated P–T pseudosection for sample JD1334 (overprinting) in the system NCKFMASHTO (+ ksp + pl + q + ilm). Others are the same as those in Fig. 6.

Fig.8 Calculated P–T pseudosection for sample JD1453 in the system NCMnKFMASHTO (+ pl + q). The circles with the labels M, N, P, A and B are corresponding to those in Table 5. Others are the same as those in Fig. 6.

Fig.9 Calculated P–T pseudosection for sample JD15126 in the system NCKFMASHTO. Mineral abbreviation: Sa – sapphirine; Others are the same as those in Fig. 6.

Fig10 Cathodoluminescence (CL) images of selected zircons from pelitic granulite samples in eastern Hebei. Solid circles shows the inner positions of LA–ICP–MS analytical sites with their identification numbers as in Supplementary Table S1, and ages in Ma, respectively.

Fig.11 U–Pb isotopic age distributions of analyzed zircons from pelitic granulites in eastern Hebei.

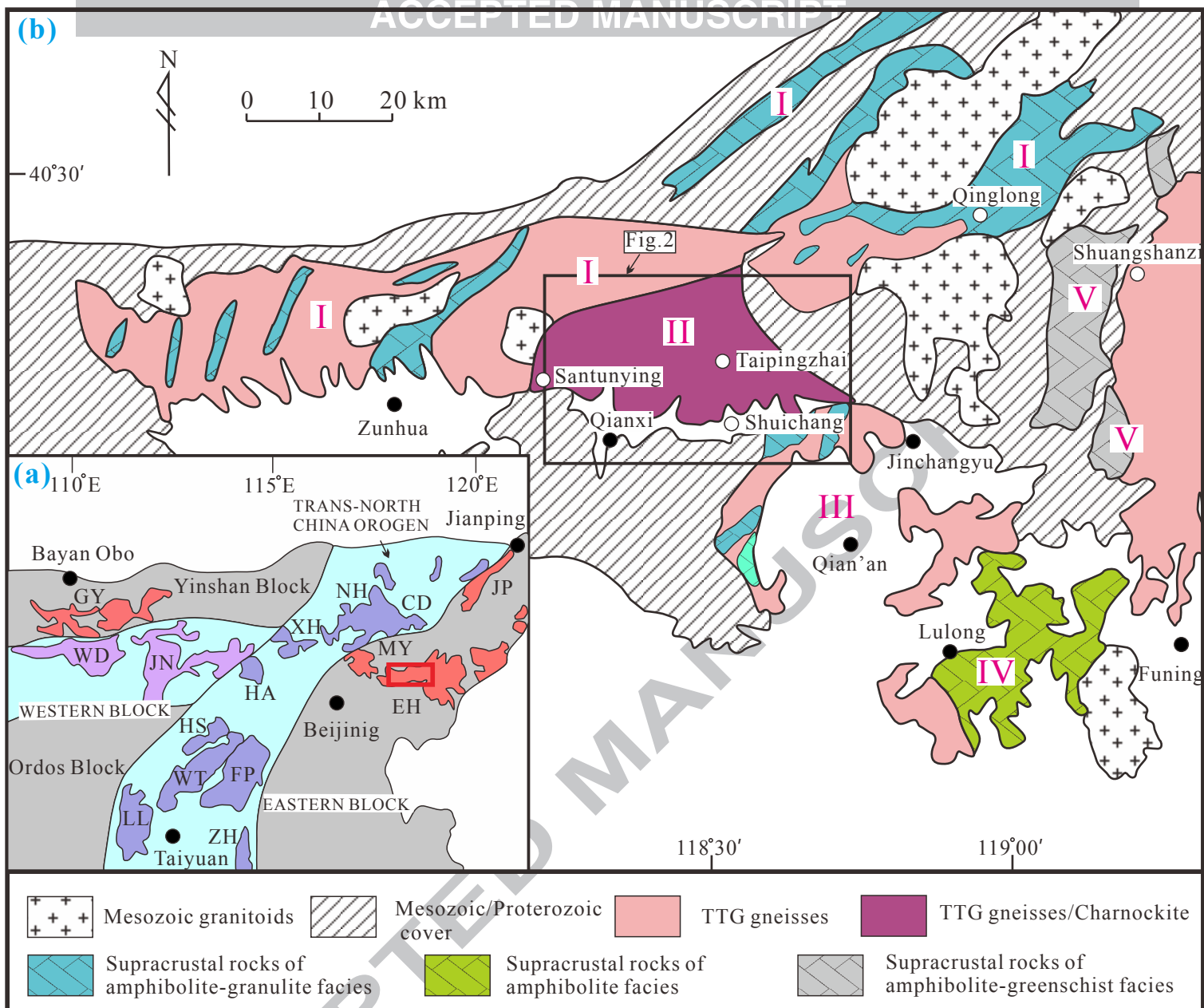
Fig.12 Chondrite-normalized REE patterns (Sun and McDonough, 1989) for zircons of magmatic (group 1), metamorphic (group 2) and complex (group 3) origin from pelitic granulites in eastern Hebei.

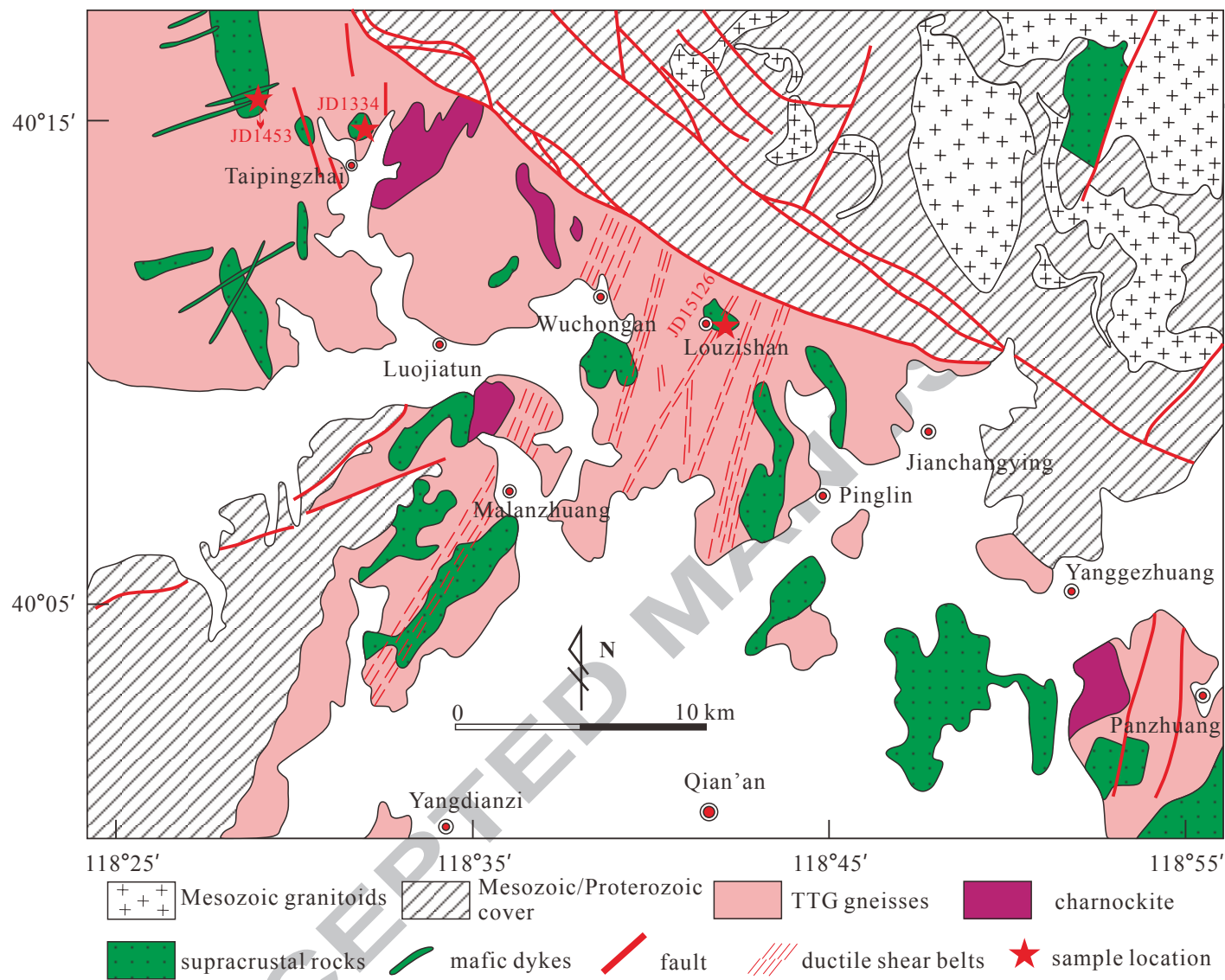
Fig. 13 The summarized P–T conditions and paths for granulites from eastern Hebei. Thick blue arrows represent the P–T paths for pelitic granulites in our study. The P–T conditions of the final assemblages for the three samples in this article are shown as the translucent boxes labelled with JD1334, JD1453 and JD15126, respectively. The P–T condition recovered from the overprinting assemblages from sample JD1334 is shown as the translucent quadrangle labelled with “Overprinting”. The P–T path labeled with Duan-15 is cited from Duan et al. (2015) for metabasic dykes of high-pressure granulite-facies. The $X_{An} = 43–45$ isopleths are from sample JD1453. The abbreviations are as follows: NG – ‘normal’ granulite; UHTG – ultrahigh-temperature granulite; E-HPG – eclogite-high-pressure granulite. The areas of NG, UHTG and E-HPG are cited from Brown (2007). The granite solidus and the disappearance of amphibole (amp-out) in tholeiite composition are adopted from Moyen and Stevens (2006). Mu-out line is from Spear and Cheney (1989). The lines of Ti-biotite-out (Ti-bi-out in pelite and Ti-bi-out in greywacke) are from Stevens et al.

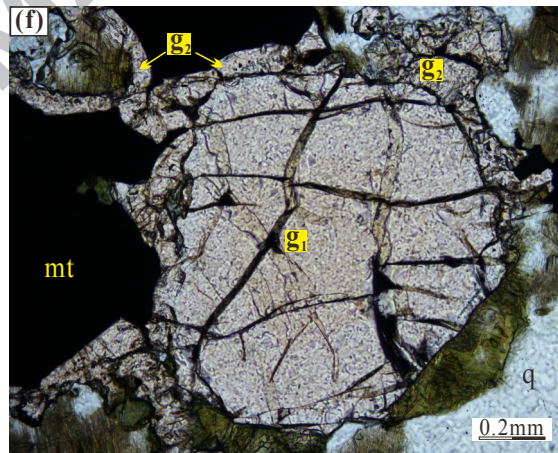
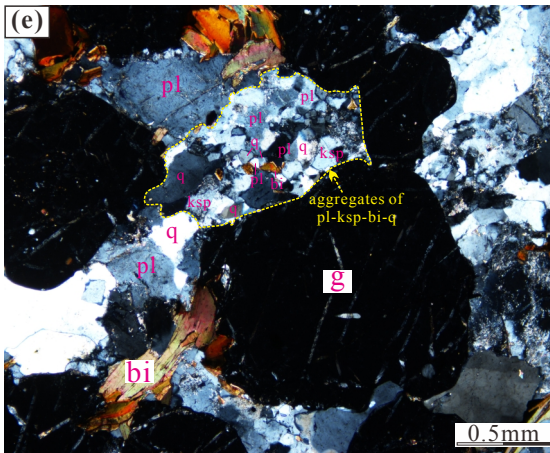
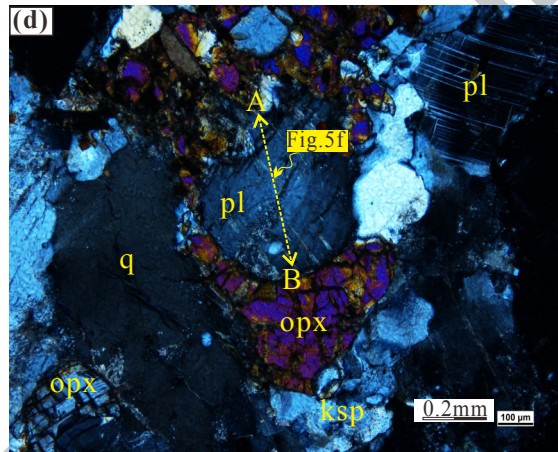
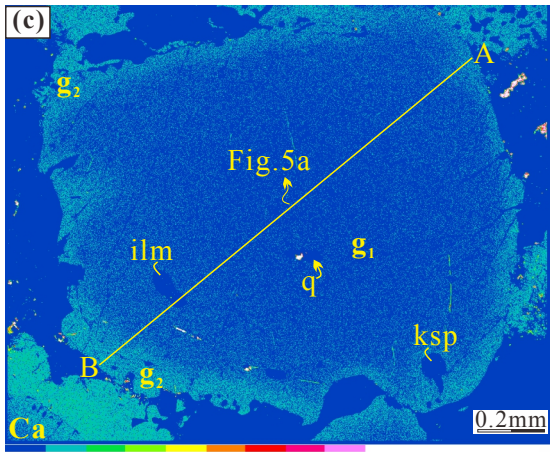
(1997). The dry solidus of granodiorite is cited from Robertson and Wyllie (1971).

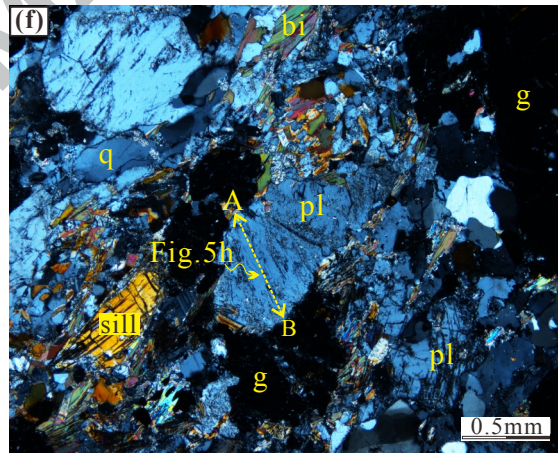
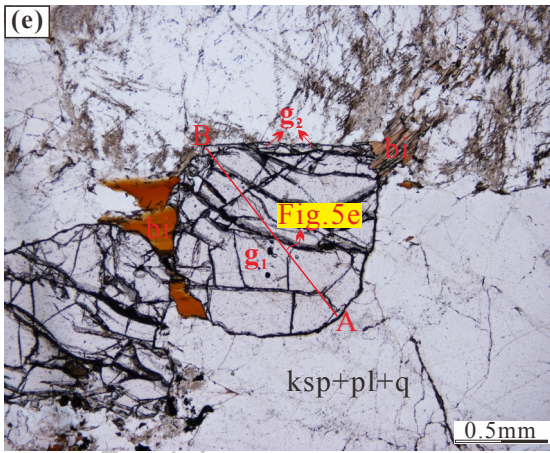
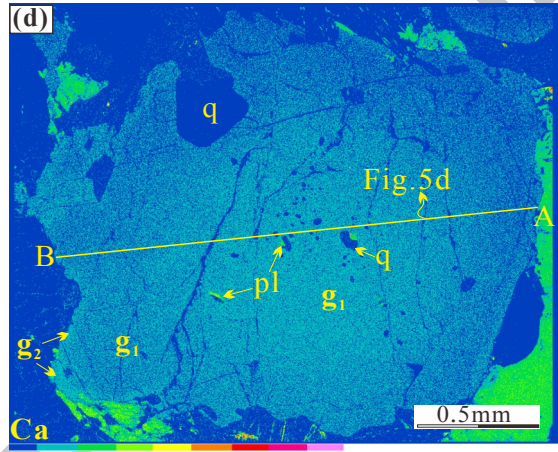
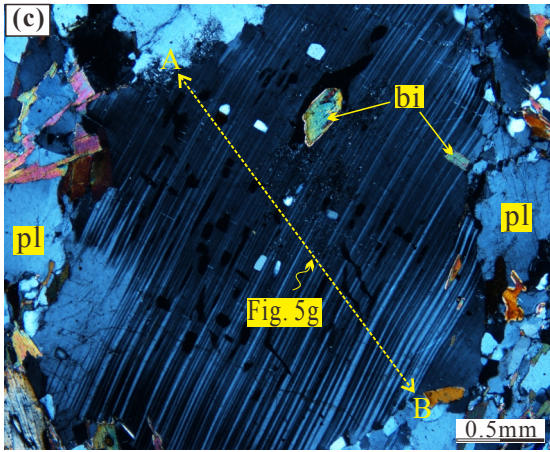
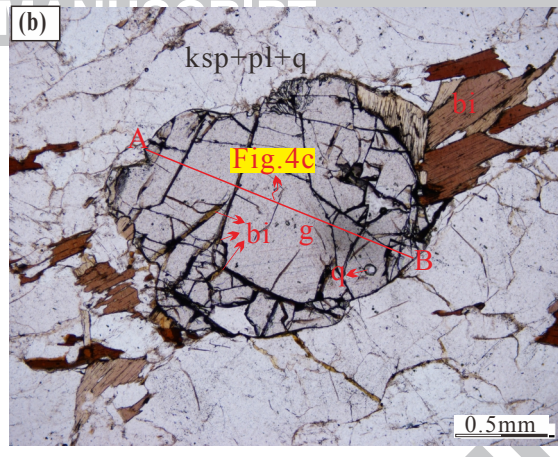
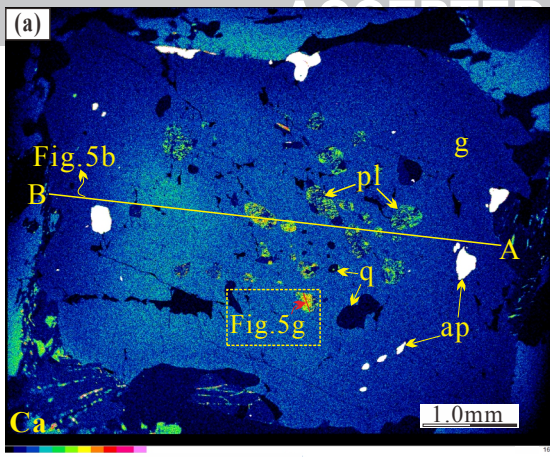
The transition lines of Al_2SiO_5 are calculated by THERMOCALC.

ACCEPTED MANUSCRIPT

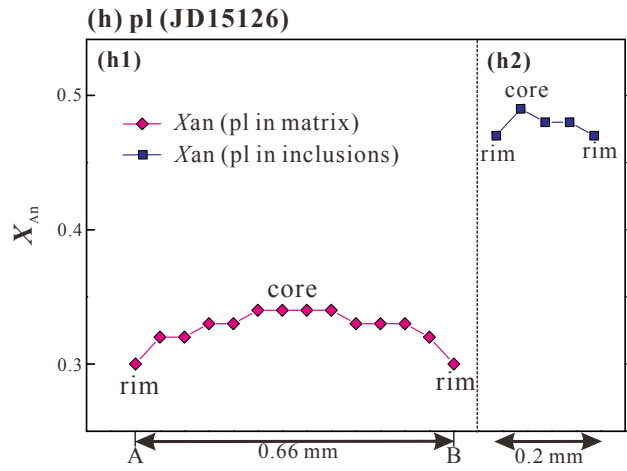
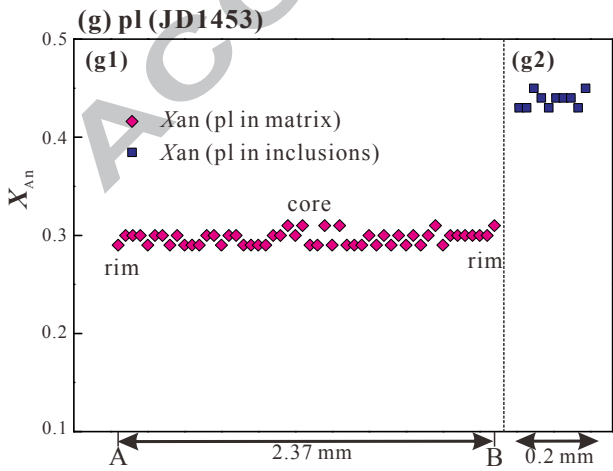
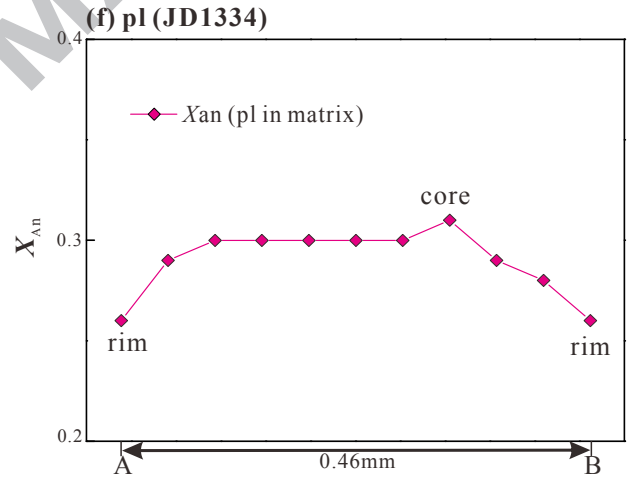
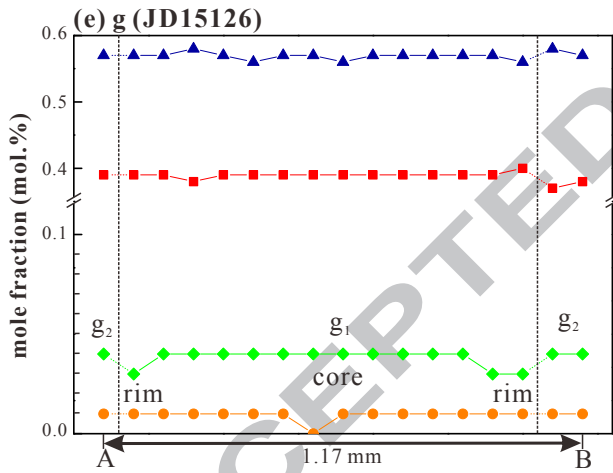
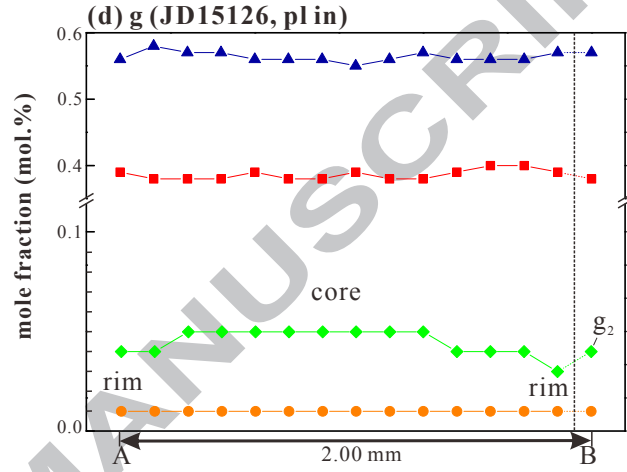
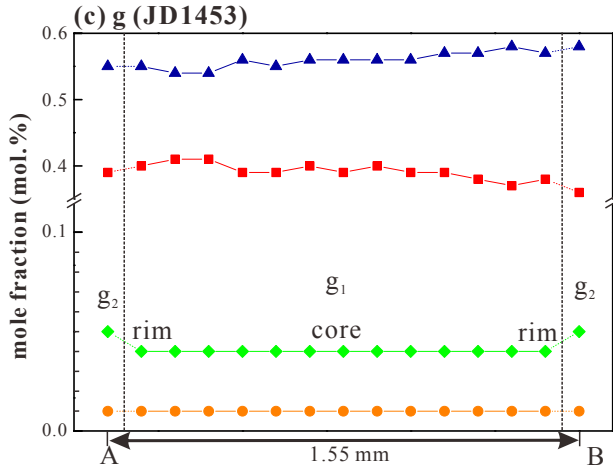
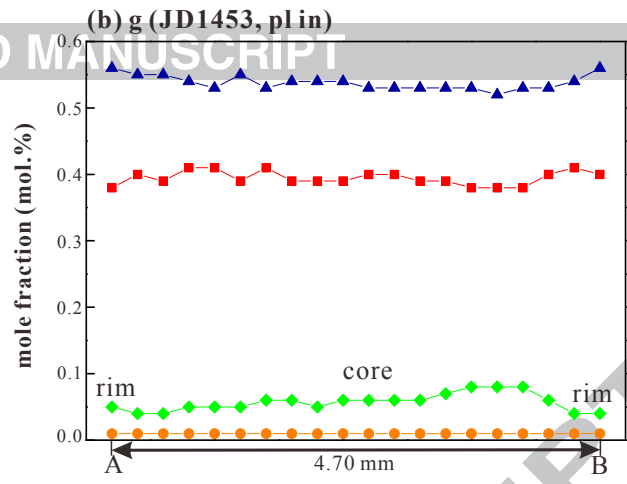
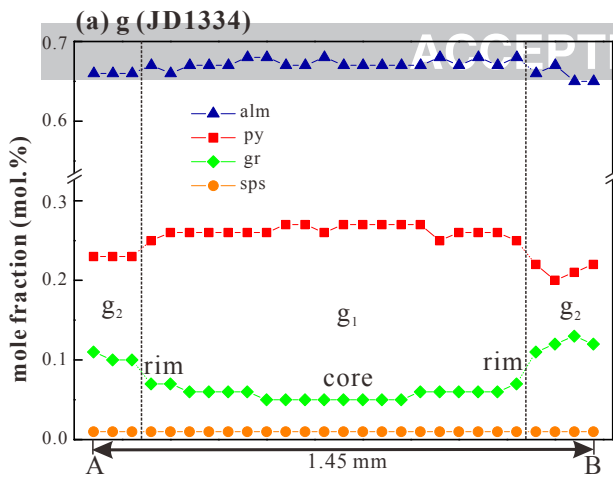


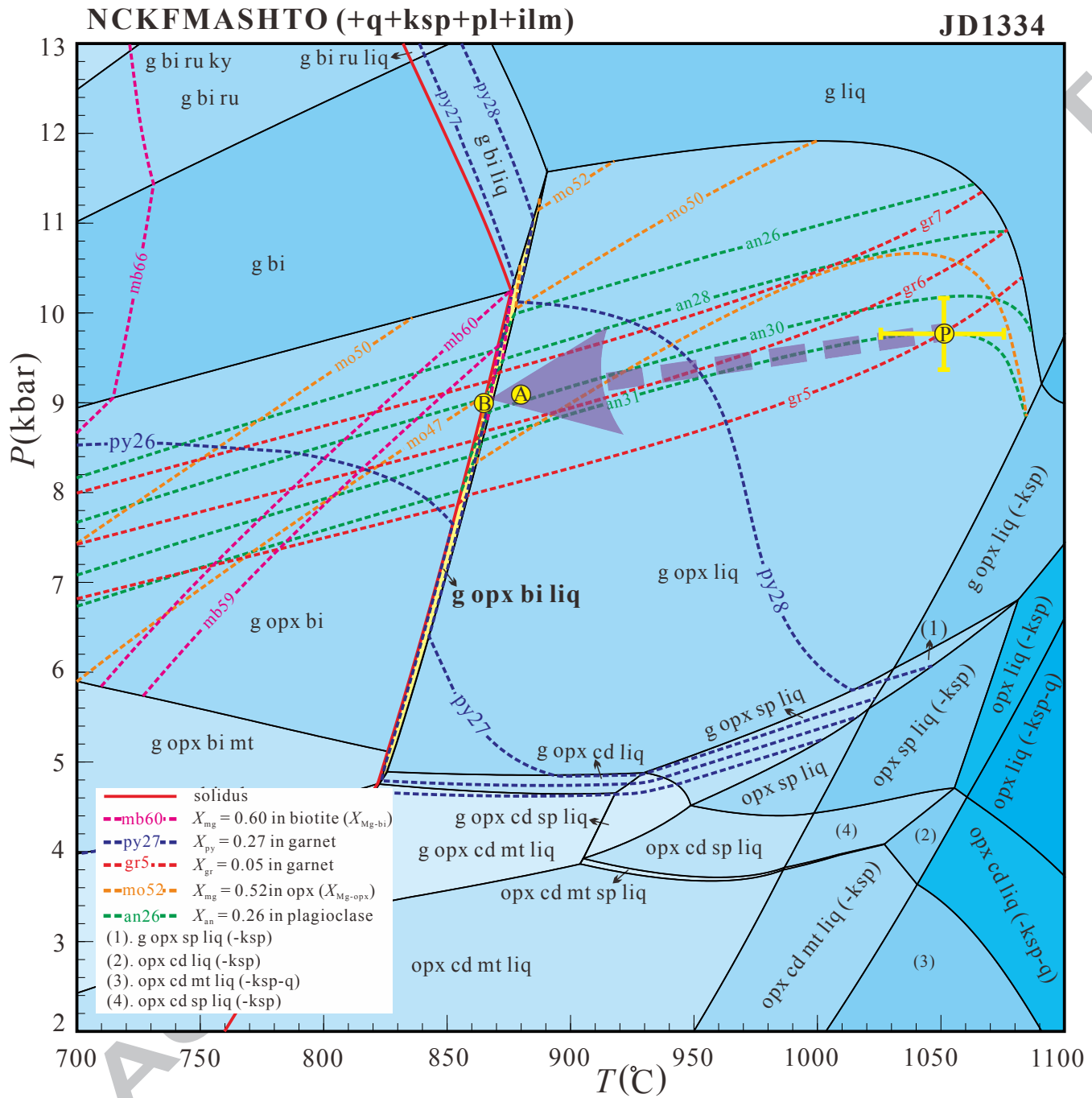


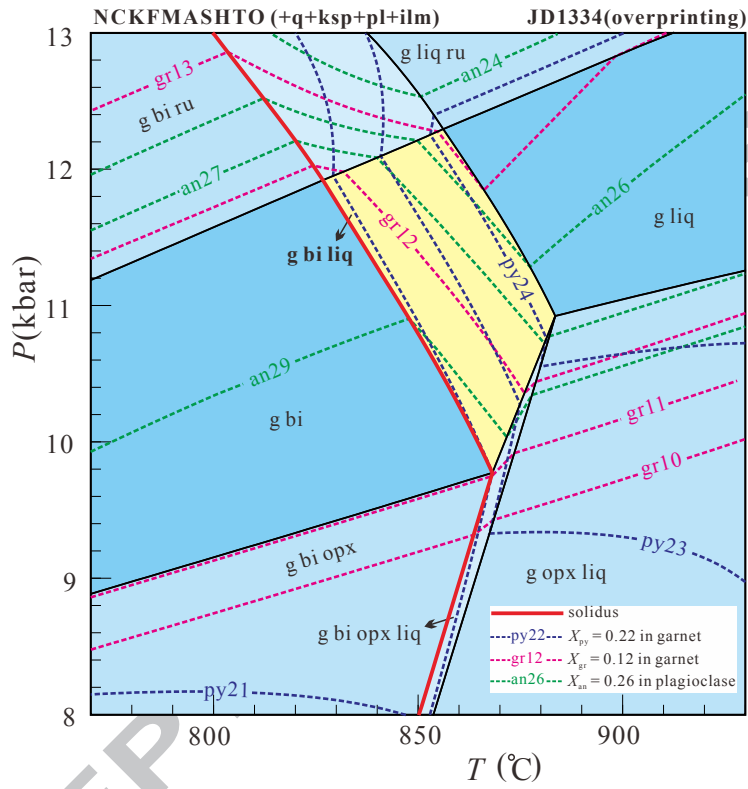


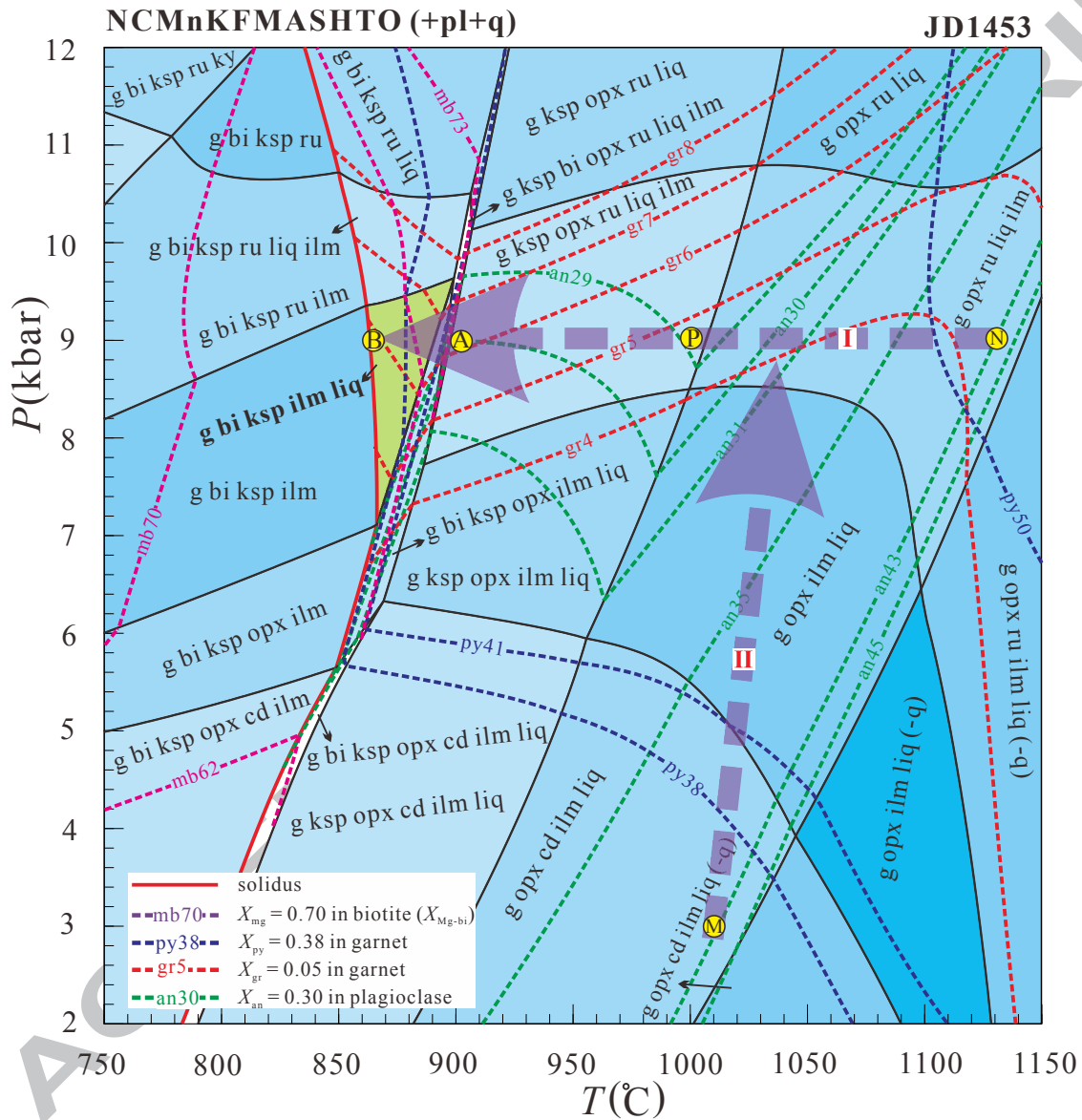


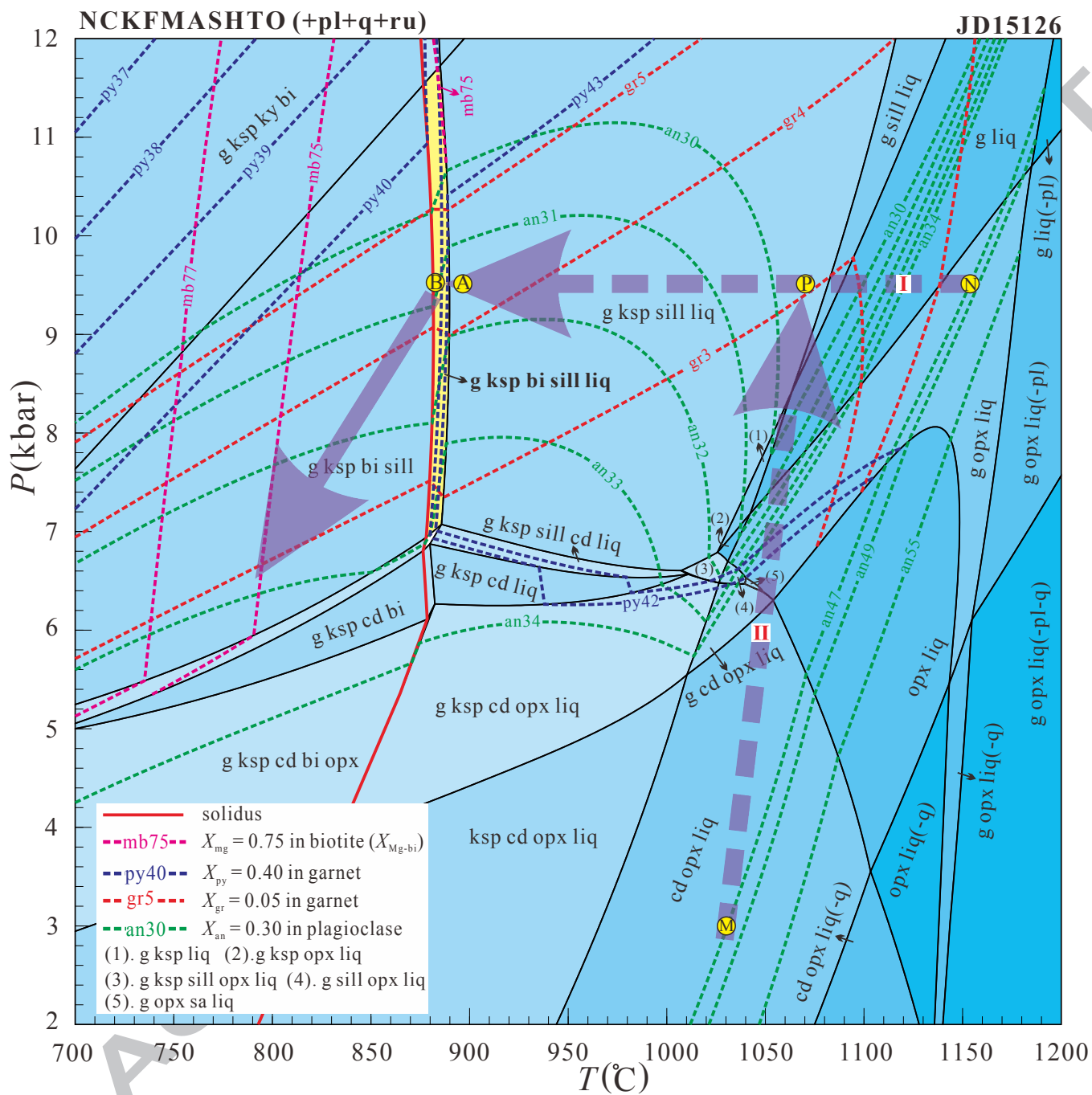
ACC



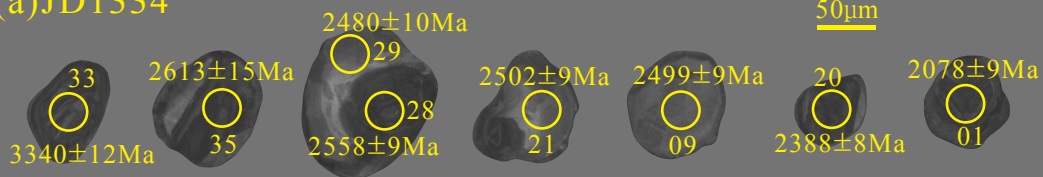








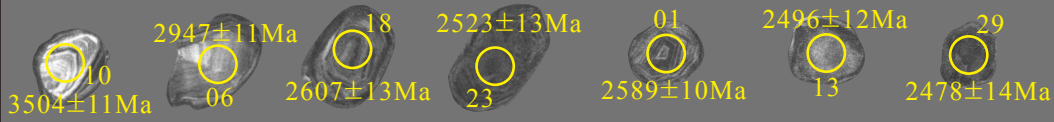
(a) JD1334



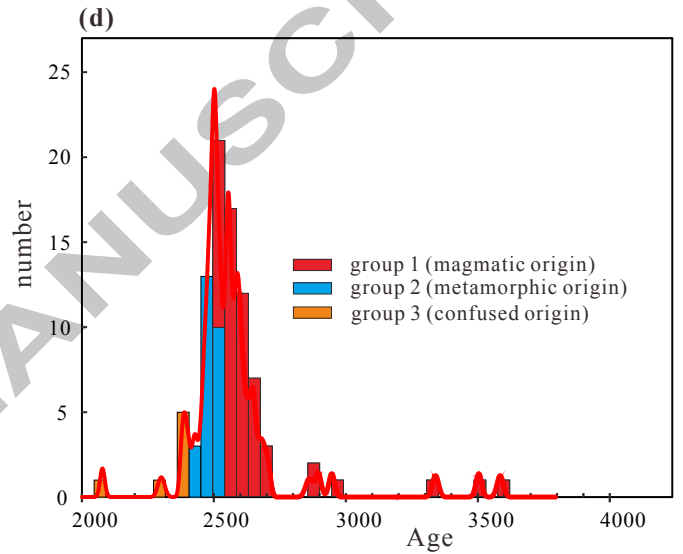
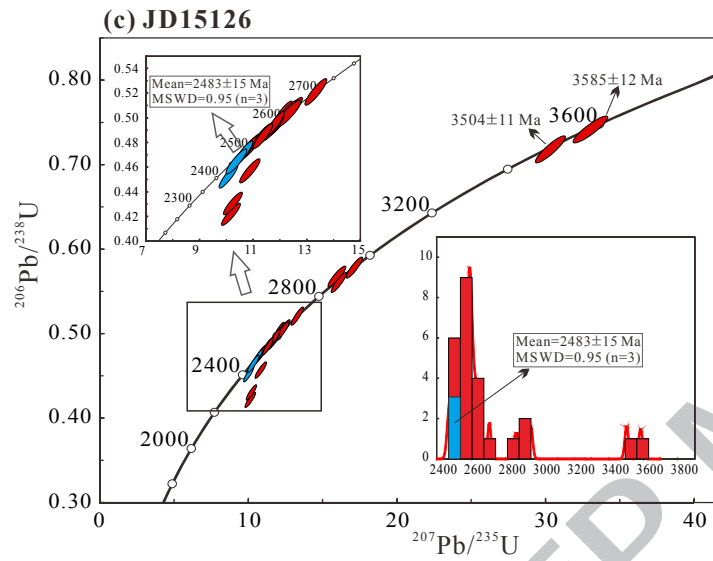
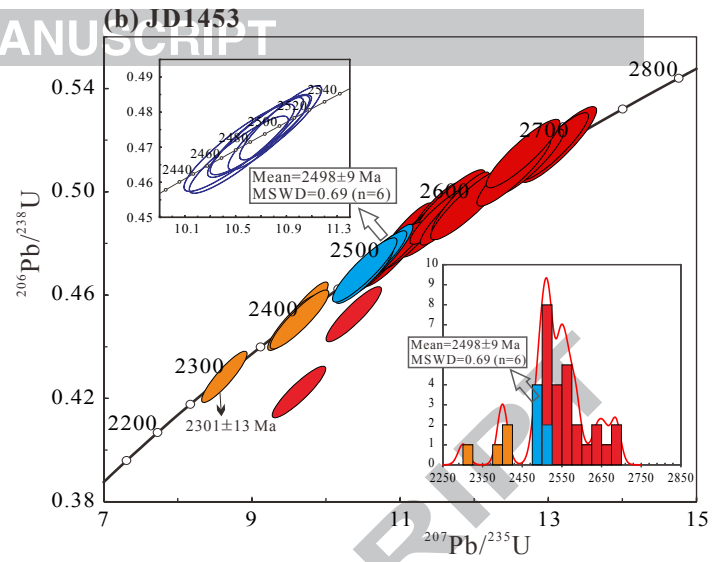
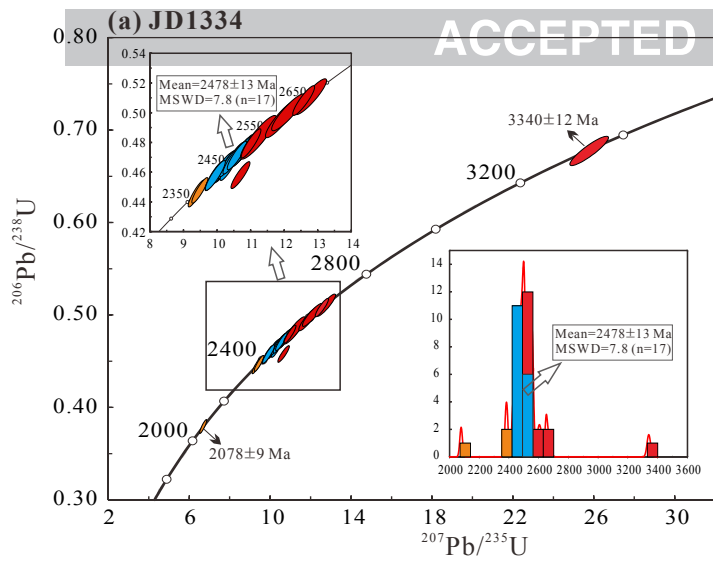
(b) JD1453

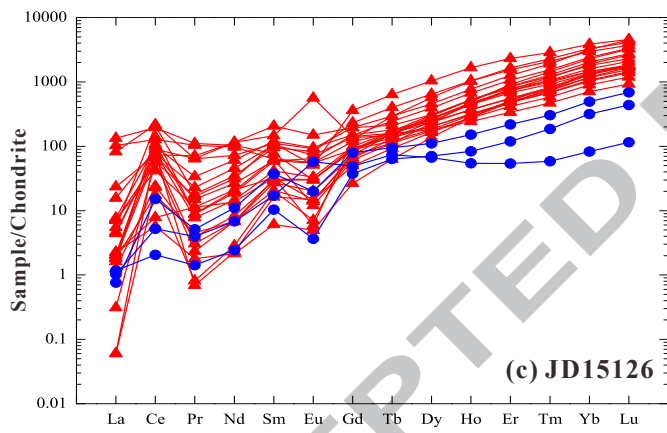
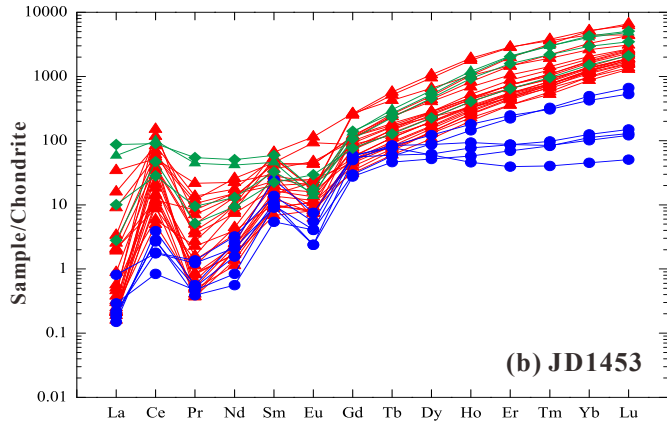
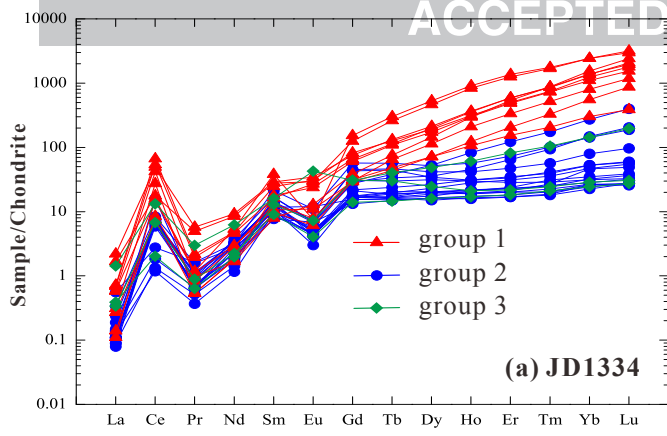


(c) JD15126



ACCEPTED MANUSCRIPT





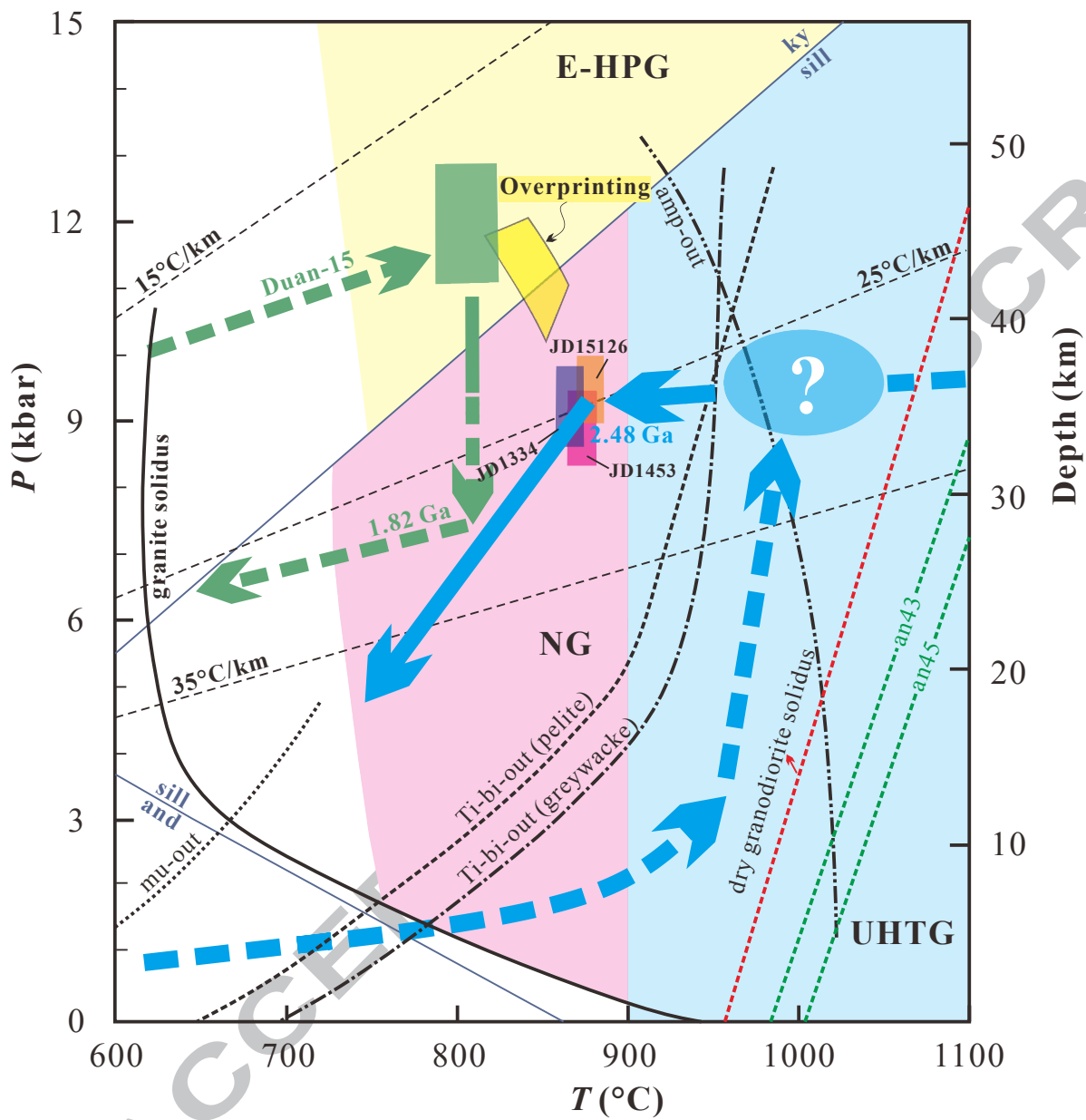


Table 1. Main mineral components, modal proportion (vol. %) and their locations of pelitic granulites from eastern Hebei

| sample | location | garnet | biotite | sillimanite | K-feldspar | plagioclase | orthopyroxene | quartz | rutile | ilmeneite | pyrite |
|---------|------------------------------------|----------|---------|-------------|------------|-------------|---------------|--------|--------|-----------|--------|
| JD1334 | 40°14.7 5'N, 118°31. 12'E | 25 | 3 | - | 16 | 30 | 2 | 23 | - | 1 | + |
| JD1453 | 40°15.4 9'N, 118°28. 78'E | 12 | 10 | - | 5 | 50 | - | 23 | - | + | - |
| JD15126 | 40°10.7 2'N, 118°41. 92'E | 21. 5 | 3 | 2 | 11 | 32 | - | 30 | 0.5 | - | - |

-, absent and +, present (< 0.5 vol. %).

Table 2. Bulk-rock compositions of pelitic granulites from eastern Hebei

| ICP-OES whole rock compositions (wt. %) | | | | | | | | | | | | | |
|---|------------------|------------------|--------------------------------|--------------------------------|------|------|-------|-------------------|-------------------|-------------------------------|------|-------|-----------------|
| Sample | SiO ₂ | TiO ₂ | Al ₂ O ₃ | Fe ₂ O ₃ | MnO | MgO | CaO | Na ₂ O | K ₂ O | P ₂ O ₅ | LOI | A/CNK | Mg [#] |
| JD1334 | 58.32 | 0.72 | 16.43 | 13.83 | 0.12 | 3.02 | 2.72 | 2.22 | 2.12 | 0.12 | 0.22 | 1.48 | 30 |
| JD1453 | 62.74 | 0.79 | 17.41 | 5.97 | 0.06 | 3.17 | 3.46 | 3.68 | 1.65 | 0.14 | 0.41 | 1.23 | 52 |
| JD15126 | 62.71 | 0.90 | 16.60 | 9.32 | 0.08 | 3.24 | 2.20 | 2.27 | 1.86 | 0.08 | 0.39 | 1.70 | 41 |
| Normalized molar proportion used for phase equilibria modelling | | | | | | | | | | | | | |
| Sample | Figs | H ₂ O | SiO ₂ | Al ₂ O ₃ | CaO | MgO | FeO | K ₂ O | Na ₂ O | TiO ₂ | O | MnO | |
| JD1334 | Fig. 6 | 0.38 | 65.06 | 10.53 | 2.59 | 4.89 | 11.55 | 1.69 | 2.40 | 0.72 | 0.20 | 0.00 | |
| JD1334 (overprinting) | Fig. 7 | 0.40 | 65.90 | 10.95 | 3.50 | 3.64 | 10.33 | 1.80 | 2.66 | 0.72 | 0.12 | 0.00 | |
| JD1453 | Fig. 8 | 1.21 | 67.73 | 11.15 | 3.74 | 4.99 | 5.32 | 1.37 | 3.85 | 0.48 | 0.09 | 0.08 | |
| JD15126 | Fig. 9 | 0.40 | 68.74 | 10.63 | 2.67 | 5.55 | 7.30 | 1.25 | 2.47 | 0.68 | 0.30 | 0.00 | |

Table 3. Selected microprobe analyses for pelitic granulites JD1334 and JD1453 from eastern Hebei

| JD1334 | | | | | | | | | JD1453 | | | | | | | | |
|-----------------|------------------|------------------|----------------|----|-----|-----|-----|----|------------------|------------------|----------------|----|----|----|-----|-----|----|
| Mi | g ₁ - | g ₁ - | g ₂ | bi | pl- | pl- | ks | op | g ₁ - | g ₁ - | g ₂ | bi | bi | pl | pl- | pl- | ks |
| SiO | 38. | 38. | 38. | 38 | 60. | 61. | 64. | 50 | 39. | 38. | 39. | 36 | 37 | 56 | 60. | 60 | 64 |
| TiO | 0.0 | 0.1 | 0.0 | 5. | 0.0 | 0.0 | 0.0 | 0. | 0.0 | 0.0 | 0.0 | 5. | 5. | 0. | 0.0 | 0. | 0. |
| Al ₂ | 21. | 22. | 22. | 14 | 25. | 23. | 18. | 1. | 22. | 22. | 22. | 16 | 15 | 27 | 24. | 24 | 18 |
| Cr ₂ | 0.0 | 0.0 | 0.0 | 0. | 0.0 | 0.0 | 0.0 | 0. | 0.0 | 0.1 | 0.0 | 0. | 0. | 0. | 0.0 | 0. | 0. |
| Fe | 30. | 30. | 30. | 15 | 0.0 | 0.1 | 0.0 | 28 | 26. | 27. | 26. | 10 | 14 | 0. | 0.1 | 0. | 0. |
| Mn | 0.3 | 0.2 | 0.3 | 0. | 0.0 | 0.0 | 0.0 | 0. | 0.4 | 0.4 | 0.4 | 0. | 0. | 0. | 0.0 | 0. | 0. |
| Mg | 6.9 | 6.3 | 5.2 | 12 | 0.0 | 0.0 | 0.0 | 17 | 10. | 9.8 | 10. | 16 | 13 | 0. | 0.0 | 0. | 0. |
| Ca | 1.8 | 2.4 | 4.4 | 0. | 6.7 | 5.5 | 0.0 | 0. | 1.4 | 1.4 | 1.8 | 0. | 0. | 9. | 6.5 | 6. | 0. |
| Na ₂ | 0.0 | 0.0 | 0.0 | 0. | 8.3 | 8.6 | 1.0 | 0. | 0.0 | 0.0 | 0.0 | 0. | 0. | 6. | 7.9 | 7. | 0. |
| K ₂ | 0.0 | 0.0 | 0.0 | 10 | 0.2 | 0.2 | 15. | 0. | 0.0 | 0.0 | 0.0 | 10 | 10 | 0. | 0.4 | 0. | 16 |
| Tot | 10 | 10 | 10 | 96 | 10 | 10 | 10 | 99 | 10 | 10 | 10 | 96 | 96 | 99 | 10 | 99 | 99 |
| O | 12. | 12. | 12. | 11 | 8.0 | 8.0 | 8.0 | 6. | 12. | 12. | 12. | 11 | 11 | 8. | 8.0 | 8. | 8. |
| Si | 2.9 | 3.0 | 2.9 | 2. | 2.6 | 2.7 | 2.9 | 1. | 3.0 | 2.9 | 3.0 | 2. | 2. | 2. | 2.6 | 2. | 2. |
| Ti | 0.0 | 0.0 | 0.0 | 0. | 0.0 | 0.0 | 0.0 | 0. | 0.0 | 0.0 | 0.0 | 0. | 0. | 0. | 0.0 | 0. | 0. |
| Al | 2.0 | 2.0 | 2.0 | 1. | 1.3 | 1.2 | 1.0 | 0. | 2.0 | 2.0 | 1.9 | 1. | 1. | 1. | 1.2 | 1. | 1. |
| Cr | 0.0 | 0.0 | 0.0 | 0. | 0.0 | 0.0 | 0.0 | 0. | 0.0 | 0.0 | 0.0 | 0. | 0. | 0. | 0.0 | 0. | 0. |
| Fe ³ | 0.0 | 0.0 | 0.0 | 0. | 0.0 | 0.0 | 0.0 | 0. | 0.0 | 0.0 | 0.0 | 0. | 0. | 0. | 0.0 | 0. | 0. |
| Fe ² | 2.0 | 2.0 | 2.0 | 0. | 0.0 | 0.0 | 0.0 | 0. | 1.6 | 1.7 | 1.6 | 0. | 0. | 0. | 0.0 | 0. | 0. |
| Mn | 0.0 | 0.0 | 0.0 | 0. | 0.0 | 0.0 | 0.0 | 0. | 0.0 | 0.0 | 0.0 | 0. | 0. | 0. | 0.0 | 0. | 0. |
| Mg | 0.8 | 0.7 | 0.6 | 1. | 0.0 | 0.0 | 0.0 | 1. | 1.1 | 1.1 | 1.1 | 1. | 1. | 0. | 0.0 | 0. | 0. |
| Ca | 0.1 | 0.2 | 0.3 | 0. | 0.3 | 0.2 | 0.0 | 0. | 0.1 | 0.1 | 0.1 | 0. | 0. | 0. | 0.3 | 0. | 0. |
| Na | 0.0 | 0.0 | 0.0 | 0. | 0.7 | 0.7 | 0.1 | 0. | 0.0 | 0.0 | 0.0 | 0. | 0. | 0. | 0.6 | 0. | 0. |
| K | 0.0 | 0.0 | 0.0 | 0. | 0.0 | 0.0 | 0.9 | 0. | 0.0 | 0.0 | 0.0 | 0. | 0. | 0. | 0.0 | 0. | 0. |
| X(p) | 0.2 | 0.2 | 0.2 | 0. | 0.3 | 0.2 | 0.9 | 0. | 0.4 | 0.3 | 0.3 | 0. | 0. | 0. | 0.3 | 0. | 0. |
| Y(p) | 0.0 | 0.0 | 0.1 | | | | | | 0.0 | 0.0 | 0.0 | | | | | | |

$X(g) = Mg/(Fe^{2+} + Mg + Ca)$; $Y(g) = Ca/(Fe^{2+} + Mg + Ca)$; $X(bi) = Mg/(Fe^{2+} + Mg)$; $X(opx) = Mg/(Fe^{2+} + Mg)$; $X(pl) = Ca/(Ca + Na + K)$; $X(ksp) = K/(Ca + Na + K)$; -C, core; -R, rim; -I, in garnet; -M, in matrix; -MC, grain core in matrix; -MR, grain rim in matrix. The mineral abbreviations are the same as those in Figs. 3-5.

Table 4. Selected microprobe analyses for sample JD15126 from eastern Hebei

| JD15126 | | | | | | | | |
|--------------------------------|-------------------|-------------------|----------------|-------|--------|--------|--------|-------|
| Mineral | g ₁ -C | g ₁ -R | g ₂ | bi-M | pl-I | pl-MC | pl-MR | ksp |
| SiO ₂ | 39.21 | 39.14 | 39.56 | 38.63 | 55.15 | 58.73 | 60.07 | 64.43 |
| TiO ₂ | 0.01 | 0.05 | 0.00 | 5.18 | 0.00 | 0.03 | 0.00 | 0.03 |
| Al ₂ O ₃ | 22.33 | 21.94 | 22.44 | 14.58 | 27.98 | 25.71 | 24.98 | 18.45 |
| Cr ₂ O ₃ | 0.04 | 0.06 | 0.06 | 0.04 | 0.04 | 0.00 | 0.00 | 0.02 |
| FeO | 26.13 | 26.90 | 26.39 | 9.43 | 0.00 | 0.04 | 0.10 | 0.00 |
| MnO | 0.33 | 0.29 | 0.34 | 0.04 | 0.01 | 0.01 | 0.00 | 0.05 |
| MgO | 10.01 | 10.28 | 10.28 | 16.29 | 0.03 | 0.00 | 0.00 | 0.00 |
| CaO | 1.88 | 1.22 | 1.43 | 0.00 | 10.22 | 7.45 | 6.64 | 0.07 |
| Na ₂ O | 0.00 | 0.02 | 0.00 | 0.05 | 5.96 | 7.73 | 8.24 | 1.16 |
| K ₂ O | 0.01 | 0.00 | 0.00 | 9.88 | 0.05 | 0.23 | 0.32 | 15.42 |
| Totals | 100.02 | 99.9 | 100.58 | 94.13 | 100.04 | 100.00 | 100.35 | 99.65 |
| O | 12.00 | 12.00 | 12.00 | 11.00 | 8.00 | 8.00 | 8.00 | 8.00 |
| Si | 3.00 | 3.00 | 3.00 | 2.84 | 2.49 | 2.63 | 2.67 | 2.99 |
| Ti | 0.00 | 0.00 | 0.01 | 0.29 | 0.00 | 0.00 | 0.00 | 0.00 |
| Al | 2.01 | 1.98 | 2.01 | 1.27 | 1.49 | 1.36 | 1.31 | 1.01 |
| Cr | 0.00 | 0.00 | 0.00 | 0.00 | 0.00 | 0.00 | 0.00 | 0.00 |
| Fe ³⁺ | 0.00 | 0.02 | 0.00 | 0.00 | 0.02 | 0.00 | 0.00 | 0.00 |
| Fe ²⁺ | 1.67 | 1.70 | 1.67 | 0.58 | 0.00 | 0.00 | 0.00 | 0.00 |
| Mn | 0.02 | 0.02 | 0.02 | 0.00 | 0.00 | 0.00 | 0.00 | 0.00 |
| Mg | 1.14 | 1.17 | 1.16 | 1.79 | 0.00 | 0.00 | 0.00 | 0.00 |
| Ca | 0.15 | 0.10 | 0.12 | 0.00 | 0.49 | 0.36 | 0.32 | 0.00 |
| Na | 0.00 | 0.00 | 0.00 | 0.01 | 0.52 | 0.67 | 0.71 | 0.10 |
| K | 0.00 | 0.00 | 0.00 | 0.93 | 0.00 | 0.01 | 0.02 | 0.91 |
| X(phase) | 0.38 | 0.39 | 0.39 | 0.75 | 0.49 | 0.34 | 0.30 | 0.90 |
| Y(phase) | 0.05 | 0.03 | 0.04 | | | | | |

Details are the same as those in Table 3.

Table 5. Comparisons of the calculated mineral compositions and modal proportions (on one-oxide basis) with those measured in samples

| | T P(kbar) | T (°C) | X(Copy) | X(Gr) | X _A n | X _M g-bi | Ti- bi | X Mg -op x | g | o p x | k s p | pl | q | bi | il m | li q | r u | s il l | c d |
|-------------------|--------------|-----------|---------|-------|---------------------|------------------------|-----------|---------------------|----|-------------|-------------|----|----|----|---------|---------|--------|--------------|--------|
| | | | | | | | | | | | | | | | | | | | |
| JD1334 | | | | | | | | | | | | | | | | | | | |
| in Fig.6 | | | | | | | | | | | | | | | | | | | |
| P | 9.78 | 1 | | | | | | | 3 | | 1 | 1 | 1 | | 1 | 1 | | | |
| | | 0 | 0.3 | 0.0 | 0.3 | | | 0. | 0. | 2. | 4. | 9. | 8. | | . | 1. | | | |
| | | 5 | 0 | 5 | 1 | | | 46 | 6 | 6 | 9 | 8 | 8 | 6 | | 8 | 1 | | |
| A | 9.10 | 8 | | | | | | | 3 | | 1 | 2 | 2 | | 1 | | | | |
| | | 8 | 0.2 | 0.0 | 0.3 | | | 0. | 3. | 4. | 7. | 0. | 0. | | . | | | | 2. |
| | | 8 | 8 | 6 | 0 | | | 48 | 0 | 8 | 1 | 2 | 8 | 4 | | 8 | | | 5 |
| B | 9.00 | 8 | | | | | | | 3 | | 1 | 2 | 2 | | 1 | | | | |
| | | 6 | 0.2 | 0.0 | 0.2 | 0.5 | 0.1 | 0. | 3. | 2. | 5. | 2. | 2. | | 3. | | | | 0. |
| | | 5 | 6 | 7 | 8 | 8 | 6 | 47 | 0 | 6 | 1 | 3 | 2 | 1 | | 1 | | | 7 |
| Mea sure d | | | 0.2 | 0.0 | 0.2 | 0.5 | 0.2 | 0. | 2. | 2. | 2. | 5. | 1. | | 3. | | | | |
| | | | 5-0 | 5-0 | 6-0 | 9-0 | 6-0 | 52 | 6 | 5 | 7 | 6 | 7 | | 8 | | | | |
| | | | .27 | .07 | .31 | .66 | .32 | 0 | 0 | 2 | 9 | 9 | | | 6 | | | | |
| JD145 | | | | | | | | | | | | | | | | | | | |
| 3 in Fig.8 | | | | | | | | | | | | | | | | | | | |
| M | 3.00 | 1 | | | | | | | | | 1 | 3 | | | 1 | 5 | | | |
| | | 0 | 0.3 | 0.0 | 0.4 | | | 0. | 0. | 2. | | 0. | 1. | | . | 0. | | | |
| | | 1 | 5 | 3 | 3 | | | 58 | 3 | 6 | 1 | 9 | 9 | | 1 | 0 | | | 3.26 |
| N | 9.00 | 1 | | | | | | | | | | 2 | 2 | | 0 | 6 | 0 | | |
| | | 1 | 0.5 | 0.0 | 0.4 | | | 0. | 2. | 8. | | 1. | 2. | | . | 4. | | | |
| | | 3 | 2 | 4 | 3 | | | 69 | 6 | 5 | 3 | 4 | 5 | | 5 | 5 | 2 | | |
| P | 9.00 | 1 | | | | | | | | | | 4 | 1 | | 0 | 1 | 0 | | |
| | | 0 | 0.4 | 0.0 | 0.2 | | | 0. | 4. | 6. | 1. | 4. | 4. | | . | 7. | | | |
| | | 0 | 5 | 5 | 9 | | | 71 | 6 | 4 | 0 | 5 | 7 | | 8 | 6 | 1 | | |
| A | 9.00 | 9 | | | | | | | | | | 4 | 1 | | 0 | | 0 | | |
| | | 0 | 0.4 | 0.0 | 0.3 | | | 0. | 7. | 5. | 8. | 1. | 7. | | . | 8. | | | |
| | | 0 | 3 | 6 | 0 | | | 63 | 6 | 0 | 5 | 0 | 9 | 3 | | 5 | 6 | 2 | |
| | | | | | | | | | | | 0 | 4 | | 8 | 6 | 3 | | | |

| | | | | | | | | | | | | | | |
|------|------|---|-----|-----|-----|-----|---------|----|----|----|----|----|---|----|
| | | 8 | | | | | | 1 | | 4 | 2 | 1 | 0 | |
| B | 9.00 | 6 | 0.3 | 0.0 | 0.2 | 0.6 | 0.1 | 5. | 2. | 6. | 3. | 1. | . | 0. |
| | | 7 | 7 | 6 | 9 | 8 | 9 | 7 | 2 | 9 | 4 | 0 | 4 | 1 |
| | | 5 | | | | | | 1 | 6 | 3 | 0 | 9 | 7 | 4 |
| | | | | | | | | 1 | | 4 | 2 | 1 | 0 | |
| Mea | | | 0.3 | 0.0 | 0.2 | 0.6 | | 1 | 4. | 4. | 2. | 1. | . | |
| sure | | | 8-0 | 4-0 | 9-0 | 2-0 | 0.28-0. | 6. | 1 | 4. | 2. | 1. | . | |
| d | | | .41 | .08 | .31 | .73 | 33 | 4 | 5 | 7 | 8 | 4 | 4 | |
| | | | | | | | | 0 | | 8 | 1 | 7 | 0 | |

JD15126
in Fig.9

| | | | | | | | | | | | | | | |
|------|------|---|-----|-----|-----|-----|---------|----|----|----|----|----|----|------|
| | | 1 | | | | | | 1 | 1 | 1 | | 4 | 0 | |
| M | 3.00 | 0 | | | 0.4 | | 0. | 6. | 8. | 1. | | 2. | . | 9.84 |
| | | 3 | | | 7 | | 48 | 8 | 5 | 6 | | 4 | 6 | |
| | | 0 | | | | | | 5 | 6 | 7 | | 0 | 8 | |
| | | 1 | | | | | | 1 | 5. | 6. | 1 | | 6 | 0 |
| N | 9.50 | 1 | 0.5 | 0.0 | 0.4 | | 0. | 2. | 1 | 9 | 2. | | 2. | . |
| | | 5 | 0 | 5 | 7 | | 64 | 5 | 7 | 6 | 0 | | 5 | 6 |
| | | 4 | | | | | | 9 | | 4 | | | 6 | 8 |
| | | 1 | | | | | | 2 | | 2 | | | 1 | 0 |
| P | 9.50 | 0 | 0.4 | 0.0 | 0.2 | | | 8. | 3. | 7. | 4. | | 4. | . |
| | | 7 | 5 | 3 | 9 | | | 8 | 3 | 5 | 5 | | 4 | 6 |
| | | 0 | | | | | | 9 | 6 | 4 | 1 | | 6 | 8 |
| | | 8 | | | | | | 3 | 1 | 2 | 2 | | 2. | 0 |
| A | 9.50 | 9 | 0.4 | 0.0 | 0.3 | | 0. | 1. | 5. | 7. | | | 6 | . |
| | | 5 | 3 | 4 | 1 | | 4 | 0 | 6 | 9 | | | 9 | 6 |
| | | | | | | | | 1 | 9 | 3 | 1 | | 8 | 9 |
| | | 8 | | | | | | 2 | 9. | 2 | 2 | | 0. | 0 |
| B | 9.50 | 8 | 0.4 | 0.0 | 0.3 | 0.7 | 0.1 | 7. | 1 | 7. | 9. | 3. | 1 | . |
| | | 8 | 1 | 4 | 1 | 3 | 9 | 7 | 5 | 3 | 6 | 5 | 4 | 5 |
| | | 2 | | | | | | 0 | 5 | 3 | 7 | 3 | 4 | 9 |
| | | | | | | | | 2 | | 2 | 2 | | 0 | 1 |
| Mea | | | 0.3 | 0.0 | 0.3 | 0.7 | | 8. | 8. | 7. | 8. | 3. | | . |
| sure | | | 7-0 | 3-0 | 0-0 | 5-0 | 0.23-0. | 5 | 9 | 9 | 9 | 3 | | . |
| d | | | .40 | .05 | .34 | .81 | 29 | 5 | 0 | 9 | 9 | 8 | | 5 |
| | | | | | | | | 5 | 1 | 3 | 8 | | | 8 |

Measured $X_{(py)}$ such as 0.25-0.27 refers to the range of pyrope contents in garnet grains; P, A, B, M and N correspond to labels in Figs 6, 8 and 9.

Highlights

- ▶ Neoproterozoic anticlockwise P–T path with peak condition of > 950 °C
- ▶ Paleoproterozoic metamorphism with P–T condition of 10–12 kbar/830–880 °C
- ▶ An interval of ~20 Ma between deposition and metamorphism of pelitic granulites